APL Photonics

TUTORIAL | DECEMBER 07 2023

Microcombs in fiber Fabry–Pérot cavities

Jonathan Musgrave ; Shu-Wei Huang ; Mingming Nie

APL Photonics 8, 121101 (2023)
https://doi.org/10.1063/5.0177134

Microcombs in fiber Fabry–Pérot cavities

Cite as: APL Photon. 8, 121101 (2023); doi: 10.1063/5.0177134
Submitted: 19 September 2023 • Accepted: 10 November 2023 •
Published Online: 7 December 2023

Jonathan Musgrave, Shu-Wei Huang, and Mingming Nie[a)]

AFFILIATIONS

Department of Electrical, Computer and Energy Engineering, University of Colorado Boulder, Boulder, Colorado 80309, USA

[a)]Author to whom correspondence should be addressed: Mingming.Nie@colorado.edu

ABSTRACT

Optical frequency combs, which consist of precisely controlled spectral lines covering a wide range, have played a crucial role in enabling numerous scientific advancements. Beyond the conventional approach that relies on mode-locked lasers, microcombs generated from microresonators pumped at a single frequency have arguably given rise to a new field within cavity nonlinear photonics, which has led to a robust exchange of ideas and research between theoretical, experimental, and technological aspects. Microcombs are extremely attractive in applications requiring a compact footprint, low cost, good energy efficiency, large comb spacing, and access to nonconventional spectral regions. The recently arising microcombs based on fiber Fabry–Pérot microresonators provide unique opportunities for ultralow noise and high-dimensional nonlinear optics. In this review, we comprehensively examine the recent progress of fiber Kerr microcombs and discuss how various phenomena in fibers can be utilized to enhance the microcomb performances that benefit a plethora of applications.

I. INTRODUCTION

Optical frequency combs (OFCs) are sets of equidistant spectral lines that were invented in the form of mode-locked lasers in the late 1990s.[1] As a ruler made of light, OFCs signify a revolution in precision metrology and were recognized by the Nobel Prize in Physics in 2005.[2] As an alternative to mode-locked lasers, microcombs are generated by pumping a passive high-quality (Q) tiny optical cavity called a microresonator with a resonant continuous-wave single-frequency laser, which can emit ultrafast pulses at astonishing rates (typically between 10 and 1000 GHz). Therefore, microcombs are extremely attractive for real-world applications due to their compact size and low power consumption, which are enabled by compatible photonic integration technology. Microcombs have rapidly approached the performance of traditional laser frequency combs since their invention in 2007[3] and have become a competitive light source architecture for comb enabled research fields such as optical atomic clockwork and optical frequency synthesizers.[4–10] Additionally, microcombs have also shown promise in applications including precision spectroscopy,[11–14] astro spectrograph calibration,[15,16] biomedical imaging,[17–19] optical communications,[20–27] coherent ranging,[28–30] and quantum information science.[31–36]

Microcombs based on dissipative Kerr soliton (DKS) have been realized in various platforms since the first demonstration in 2014,[37,38] including whispering-gallery microresonators[37,39–41] and microresonators based on planar waveguides[42–47] and photonic structures[48–52] fabricated in different material platforms, such as doped silica,[39] calcium fluoride (CaF_2),[41] magnesium fluoride (MgF_2),[37] lithium niobate ($LiNbO_3$),[42] aluminum nitride (AlN),[43] aluminum gallium arsenide (AlGaAs),[44] silicon nitride (Si_3N_4),[45] silicon carbide (SiC),[46] chalcogenide,[47] and so on. Recently, fiber microresonators[53–55] have received a lot of attention in the microcomb community, mainly due to their ultralow propagation loss, easy commercial access, compatibility with existing optical systems, ultralow noise enabled by the large mode volume, and multiple degrees of freedom for high-dimensional nonlinear optics. Here, we review the recent progress of fiber Kerr microcombs and discuss how various phenomena in fibers can be utilized to enhance the microcomb performances that benefit a plethora of applications.

The paper is organized as follows: Sec. II introduces fiber Fabry–Pérot (FP) microcavity, including the theory, factors affecting the cavity loss, and measurement of the cavity Q factor and dispersion. In Sec. III, we give a brief introduction to the DKS microcombs, including the governed theory and models, soliton dynamics, soliton properties, the experimental methods for soliton excitation and stabilization, and the soliton uniqueness in FP cavities. In Secs. IV and V, we focus on the fiber Kerr microcomb generation with the Brillouin effect and gain effect, respectively, from the basic mechanisms to the state-of-the-art DKS results. Of note, the discussion is not limited to the fiber microcombs but can be extended to other

microresonators. Finally, in Sec. VI, a summary and outlook of fiber microcombs are given for future studies, including new physical mechanisms and potential applications.

II. FIBER FP MICROCAVITY

As an ultralow-loss waveguide, fiber is naturally a good candidate for passive ultrahigh-Q resonators. Different forms of fiber resonators (Fig. 1) have been proposed, such as FP cavities made from fiber Bragg gratings [Fig. 1(a)][56] or free-space mirrors[57] with high reflectivity, fiber ring resonators made from directional couplers [Fig. 1(b)],[58] microfiber knot resonators [Fig. 1(c)],[59–61] and monolithic FP resonators with high-reflectivity coating at both end faces [Figs. 1(d) and 1(e)].[53–55,62–64] Among them, the last form [Figs. 1(d) and 1(e)] has been proved to have both ultrahigh Q and large comb spacing. Hence, we will focus on the dielectrically facet-coated monolithic fiber FP microresonator in the later discussion. Of note, in many published papers, fiber FP cavities are referred to as cavities where two fiber ends are coated with reflective mirrors and light propagates between them within an air gap.[65] Despite the wide applications of air-gaped microcavities in optical sensing, they cannot be used for microcomb generation due to the small nonlinearity of air. Additionally, fiber microspheres[66] are not considered here due to the large number of whispering gallery modes instead of the fiber structures that determine spatial modes.

A. Theory of fiber FP cavity

A typical FP cavity is created by trapping optical energy in an enclosed optical path $2nL$ (n is the optical refractive index of the intracavity media, L is the cavity geometric length) with two highly reflective mirrors. The light field circulating back and forth between the mirrors experiences constructive interference when the roundtrip path covers an integer number of wavelengths, $N \cdot \lambda = 2nL$. The wavelengths that exactly satisfy the above-mentioned equation are the longitudinal modes of the FP cavity, corresponding to the optical frequency through $\nu = c/n\lambda$, where c is the speed of light. The frequency difference, $\Delta\nu_{FSR}$, between adjacent longitudinal modes is called the free spectral range (FSR), or later the comb spacing, and can be calculated as $\Delta\nu_{FSR} = c/2nL$. Of note, the complete symbol definition in this tutorial can be found in Nomenclature.

The complex amplitude of the transmitted field can be described by its relationship to the input field A_0 as

$$A_t = \frac{Te^{-\frac{i\phi}{2}}e^{-\frac{\alpha L}{2}}}{1 - Re^{-i\phi}e^{-\alpha L}}A_0, \tag{1}$$

where α is the propagation loss, T and R are the transmission and reflectivity coefficients of the optical power subject to the relationship $T + R = 1 - \alpha$ and are assumed to be equivalent on both end faces. $\phi = 4\pi nL/\lambda$ is the total accumulated roundtrip phase. As shown in Fig. 2, increasing the mirror reflectivity results in a narrower linewidth of the transmitted Lorentz curve as well as a higher extinction ratio (ER).

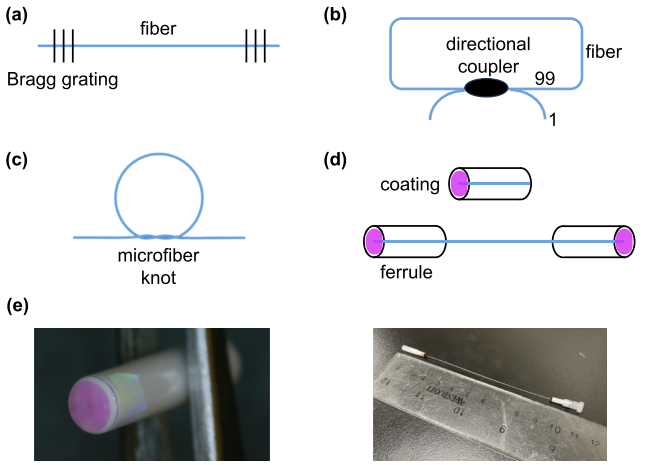

FIG. 1. Different forms of passive fiber resonators. (a) Fiber FP resonators made from fiber Bragg gratings. The reflectivity of Bragg grating is limited, and the grating length is usually large. (b) Fiber ring resonators made from directional couplers. Both insertion loss in the directional coupler and bending loss in the fiber prevent high-Q fiber microresonators. (c) Evanescent coupling enabled microfiber knot resonators. (d) Dielectrically facet-coated monolithic fiber FP resonators. Top: with a large FSR; bottom: with a small FSR. (e) Pictures of dielectrically facet-coated monolithic fiber FP resonators with FSRs of 10-GHz (left) and 1-GHz (right). The length of the ferrule is only a few millimeters. Left of (e) is adapted from Ref. 54.

B. Cavity loss

The monolithic fiber FP microresonator did not come back into the view of the nonlinear optics community until 2009,[62] which was 30 years after its first application for optical sensing in 1979.[67–69] During this long period, the development of fabrication techniques makes possible a fiber FP microresonator with ultralow loss and an ultrahigh Q factor. Monolithic fiber FP microresonators are usually fabricated through three steps:[54,55,70] (i) fiber is carefully cleaved and encapsulated in a ceramic fiber ferrule; (ii) both fiber ends are mechanically polished to subwavelength smoothness; and (iii) both fiber ends are coated with an optical dielectric Bragg mirror (DBR) with high reflectivity.

The ultralow loss results in photon storage at a long time scale, which greatly increases the intracavity power and is the premise for nonlinear cavity studies. The loss can be characterized by several related parameters, such as quality factor Q, finesse F, cavity linewidth $\Delta\nu$, and cavity photon lifetime τ. The definition and relationships between them are

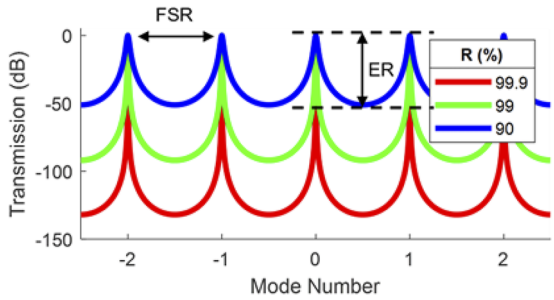

FIG. 2. Calculated transmission of a FP cavity with different mirror reflectivity.

$$Q = \nu/\Delta\nu = 2\pi\nu \cdot \tau, \tag{2}$$

$$F = \Delta\nu_{FSR}/\Delta\nu. \tag{3}$$

Therefore, lower loss leads to a longer photon lifetime, narrower cavity linewidth, higher finesse, and higher Q. The intracavity power enhancement factor with respect to the pump is F/π, which verifies ultralow loss can lead to high intracavity power.

The total loss is divided into the output coupling loss α_o and the intrinsic loss α_i. According to the fabrication process, the output coupling loss comes from the designed DBR transmission loss. There are many factors affecting the intrinsic loss, for example, the absorption and scattering loss induced by defects in the fiber [Fig. 3(a)] or at the fiber end. There are three other dominant origins for intrinsic loss, such as thick coating layers [Fig. 3(b)], tilted layers [Fig. 3(c)], and imperfect angle-cleaving at the fiber end faces [Fig. 3(d)]. These errors can prevent 100% of the light from reflecting back into the fiber due to either diffraction or an optical path mismatch. The bending loss is usually neglected. Of note, a fiber FP resonator made from graded-index fiber has a better tolerance to the above-mentioned three factors thanks to the large core size and thus can achieve a finesse of $>10^4$ and a measured loaded Q factor of $>10^8$ with an FSR of ~10 GHz.[54]

To achieve efficient loading from an external pump into the resonator, the output coupling loss should match the intrinsic loss. Depending on the relationship between α_o and α_i, three cases can be classified: critical coupling ($\alpha_o = \alpha_i$), undercoupling ($\alpha_o < \alpha_i$), and overcoupling ($\alpha_o > \alpha_i$). For the critically coupled case, the light can be efficiently stored in the microresonator, and no pump light transmits through the coupling port. For the undercoupled case, part of the light transmits through the coupling port with no phase change compared to the pump. For the overcoupled case, part of the light transmits through the coupling port with a π phase change compared to the pump. As for FP resonators, if coupled from one port, the other port then contributes to the intrinsic loss. Therefore, only under coupling is possible in FP cavities when both end-facets have the same DBR transmission and there is non-zero intrinsic loss from other contributions.

C. Measurement of Q factor

According to Eq. (2), there are two methods to measure the loaded Q factor (Q_L, including both the coupling loss and the intrinsic loss): (i) measure the cavity linewidth in the frequency domain; (ii) measure the photon lifetime in the time domain. In order to measure the cavity linewidth, the frequency of a low-power single-frequency laser is scanned across the cavity resonance at the center wavelength under test. At the same time, the scanned frequency is calibrated by a frequency reference such as a Mach–Zehnder interferometer (MZI) with a known FSR, converting the temporal signal into the frequency information. As illustrated in Fig. 4(a), the cavity linewidth is obtained from the full width at half maximum (FWHM) of the fitted Lorentz transmission spectrum. The other method is the cavity ring-down method, which measures the photon lifetime [Fig. 4(b)]. This is simply performed by loading the cavity at resonance, then removing the pump and recording the decay time of the intracavity intensity. Of note, the cavity photon lifetime is defined as the decay time of the stored energy to 1/e (≈37%) of its initial value.

D. Measurement of dispersion

The group velocity dispersion (GVD) is defined as the frequency dependence of the group velocity in a medium, or quantitatively, the derivative of the inverse group velocity with respect to angular frequency. The GVD is one of the most important parameters for broadband DKS comb generation since it causes FSR differences for different center wavelengths and the temporal walk-offs of different frequency components for an ultra-short pulse in a resonator. The GVD is determined by both the material and geometry, such as the waveguide curvature, size, thickness, and angle, which can be numerically designed by commercially available software (e.g., COMSOL Multiphysics).

The GVD of an optical waveguide can be measured by the spectral interferometric method. As shown in Fig. 5(a), a broadband laser source is directed into a Michelson interferometer, where the sample arm contains the waveguide under test. The reference arm is in free space with a movable reflective mirror, which is responsible for precisely adjusting the optical path length difference between the two

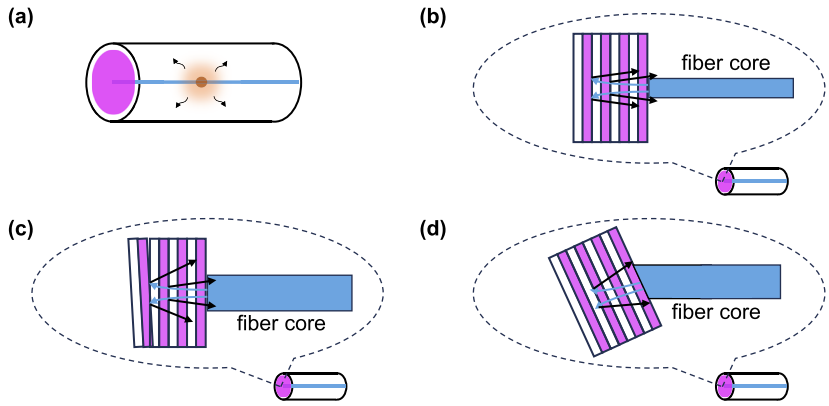

FIG. 3. Factors affecting the intrinsic loss of the dielectrically facet-coated monolithic fiber FP resonator. (a) Scattering loss and absorption loss in the fiber or on the coating; (b) induced diffraction loss by thick coating layers; and induced optical path change by (c) tilted coating layers[71] or (d) angle-cleaved fiber end faces.

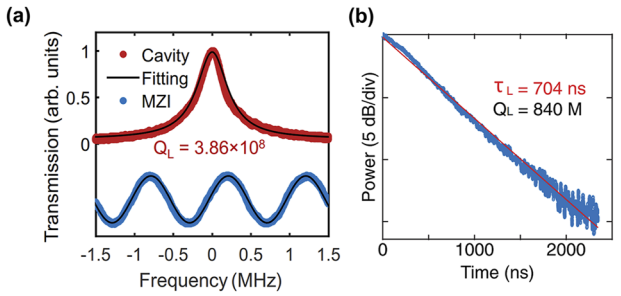

FIG. 4. Q factor measurement. (a) Cavity linewidth measurement; (b) cavity photon lifetime measurement by the cavity ring-down method. Adapted from Refs. 54 and 72.

arms. Reflected light beams in the two arms coincide through the 50/50 beam splitter and are collected into an optical spectrum analyzer (OSA) through a single-mode fiber. The interference pattern takes the form

$$I(\omega) \sim 1 + \cos[\phi(\omega)], \tag{4}$$

where $\phi(\omega)$ is the phase difference between the two arms and is related to the cavity's wave vectors and the difference between the free space propagation length as

$$\phi(\omega) = 2[\beta_w(\omega)L_w - \beta_{FS}(\omega)\Delta L_{FS}]. \tag{5}$$

Here, $\beta_w(\omega)$ and $\beta_{FS}(\omega)$ are propagation constants in waveguide and free space, respectively. In addition, ΔL_{FS} is the difference in free space between the sample and reference arms, and L_w is the waveguide length. The phase can be Taylor expanded around ω_0 as

$$\phi(\omega - \omega_0) = \phi_0 + 2\big[(\beta_1(\omega_0)L_w - \Delta L_{FS}/c)(\omega - \omega_0) + \beta_2(\omega_0)L_w(\omega - \omega_0)^2 + \cdots\big]. \tag{6}$$

The dispersion of the waveguide can be retrieved by fitting the spectral interference pattern, as shown in Figs. 5(b) and 5(c). According to this equation, a longer waveguide and a broader white-light source are required to measure lower dispersion.

The dispersion can also be measured in resonator form by measuring the resonant eigen-frequencies, which are described as a Taylor expansion around the center frequency as

$$\omega_\mu = \omega_0 + \sum_j \frac{D_j \mu^j}{j!}. \tag{7}$$

Here, D_j corresponds to the order of the cavity dispersion; D_1 is FSR, and D_2 is GVD. To obtain the resonant frequencies, the wavelength of a low-power single-frequency pump laser is scanned across the cavity resonances. Several calibrated frequency references can be utilized to reveal the sweeping nonlinearity and determine the actual wavelength of the sweeping laser, such as a laser wavelength meter, a mode-locked fiber frequency comb, an electro-optic modulated frequency comb, or a fiber MZI.[73] Among these references, the fiber MZI is the most convenient and cheapest reference. However, the dispersion of fiber MZI should be compensated[55] across a wide wavelength range, and the FSR of the fiber MZI should be calibrated, for example, using a wavelength reference before use. Besides, it is better to enclose the MZI and conduct the dispersion measurement at a relatively fast speed to avoid environmental perturbation.

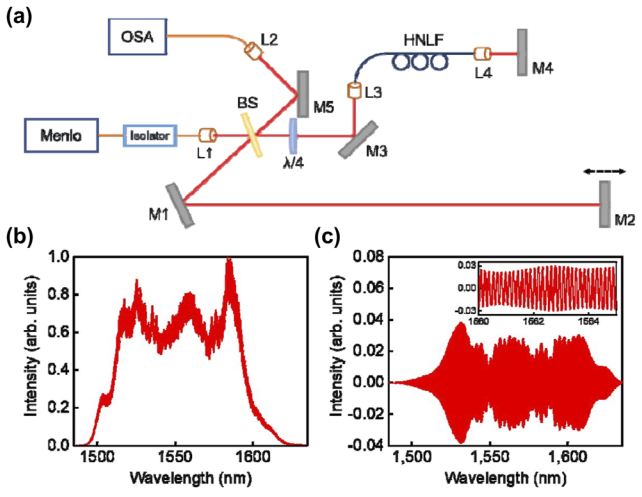

FIG. 5. Measuring the dispersion of a highly nonlinear fiber (HNLF). (a) Experimental setup of a Michelson interferometer, a broad-spectrum pulsed laser-source (Menlo) is split in the beam splitter (BS) into the sample and reference arm. The reference arm is reflected by a tunable delay mirror (M2) to accurately control the pulse overlap in time. In the sample arm, the pulse is coupled to the fiber under test through a lens (L1) and experiences an additional spectral phase through the double pass in the HNLF. OSA: optical spectrum analyzer; M1–M4: mirror; L1–L4: lens. (b) The captured spectrum shows the interferogram superimposed on the Menlo spectrum. (c) Interference spectrum after the FFT filter. Adapted from Ref. 63.

III. INTRODUCTION TO DISSIPATIVE KERR SOLITON

A. Principle of dissipative Kerr soliton generation in passive ring microresonators

In a conservative system, such as a loss-less fiber, a soliton is formed due to the balance between the Kerr nonlinearity and anomalous dispersion. In most materials, the Kerr nonlinearity leads to self-phase modulation (SPM), which causes the leading edge of a pulse to shift to longer wavelengths and the trailing edge to shift to shorter wavelengths. In addition, in a material with anomalous quadratic dispersion, blue-shifted frequencies travel faster than red-shifted frequencies. As a consequence, the newly generated frequencies on the leading and trailing edges from Kerr nonlinearity tend toward the center of the pulse due to the dispersion effect. This leads to a self-organized stable pulse, a conservative soliton that balances dispersion and nonlinearity. According to the theoretical analysis, a soliton has a sech^2-shape pulse profile and sech^2-shape spectrum. Of note, a pure-quartic soliton[74,75] is feasible due to the balance between Kerr nonlinearity and negative quartic dispersion when the low-order dispersion is neglected through critical dispersion engineering.

Dissipative Kerr soliton (DKS) frequency microcombs in high-Q microresonators are another example of self-organization in driven dissipative nonlinear systems. Compared to the conservative

soliton, DKS formation not only relies on the balance between nonlinearity and dispersion but also on the balance between dissipation and gain. The DKS dynamics in the ring resonator is described by the Lugiato–Lefever equation (LLE), where high order effects are neglected,[76,77]

$$t_R \frac{\partial A}{\partial t} = -\left(\alpha + i\delta + i\frac{\beta_2 L}{2}\frac{\partial^2}{\partial \tau^2}\right)A + i\gamma L|A|^2 A + \sqrt{\kappa_{ex}}A_p, \quad (8)$$

where A is the intracavity field, A_p is the amplitude of the incident pump field, t_R is the round-trip time, t is the slow time variable, τ is the fast time that corresponds to the local time within the cavity, α is the total round-trip loss, δ is the detuning of the cavity resonance from the pump frequency, L is the cavity length, β_2 is the group velocity dispersion (GVD) of the microresonator (anomalous dispersion: $\beta_2 < 0$, normal dispersion: $\beta_2 > 0$), γ is the Kerr nonlinear parameter, and κ_{ex} is the pump coupling coefficient. The LLE was first introduced in 1987 by Luigi Lugiato and Ren'e Lefever to analyze spatiotemporal pattern formation in a continuous-wave (CW)-driven, dissipative, diffractive, and nonlinear optical cavity.[76] This mean-field equation combines the well-known nonlinear Schrödinger equation with the boundary conditions under the good cavity approximation.[77] The LLE can also be normalized from Eq. (8) by replacing $\alpha t/t_R \to t$, $\delta/\alpha \to \delta$, $\tau\sqrt{\alpha/L} \to \theta$, $A\sqrt{\alpha/\gamma L} \to \psi$, and $A_p\sqrt{\kappa_{ex}/\alpha\gamma L} \to S$. The normalized form reads as[78]

$$\frac{\partial \psi}{\partial t} = -\left(1 + i\delta + i\frac{\beta_2}{2}\frac{\partial^2}{\partial \theta^2}\right)\psi + i|\psi|^2\psi + S, \quad (9)$$

where ψ is the intracavity field, S is the amplitude of the incident pump field, t is the slow time variable, and θ is the cavity phase coordinate. The second term after the bracketed term on the right-hand side of Eq. (9) represents the self-phase modulation induced phase shift. In Eqs. (8) and (9), the pump can be either a continuous-wave or a pulse with a repetition rate synchronized to the cavity FSR. Of note, Kerr nonlinearity can be negative from cascaded quadratic processes[79,80] and be balanced by normal dispersion to form a DKS. Of note, there are some differences in LLE for FP resonators due to the counterpropagating fields (see Sec. III D for details).

Unlike the LLE, which describes the comb dynamics in the time domain, the coupled mode equations (CME) describe the mode interactions through four-wave mixing in the frequency domain.[37] In theory, the LLE and CME are equivalent theoretical models.[81] Numerical solutions of both the LLE and CME can be numerically solved through the split-step Fourier method, which allows computationally efficient modeling of octave-spanning microcombs even on a consumer-grade computer. However, it is more straightforward to include some nonlinear effects such as the Raman effect[82] in the LLE, while it is beneficial to include avoided mode crossings (AMXs) or the Brillouin effect[83] in the CME.

We will conclude this section with some deep physical insights according to the normalized LLE. The first is the induced optical bistability. By setting all the derivatives to zero in Eq. (9), the relationship between the input and the intracavity homogeneous solution is given by

$$S^2 = \left[1 + \left(|\psi|^2 - \delta\right)^2\right]|\psi|^2. \quad (10)$$

When $\delta > \sqrt{3}$, single input leads to three possible system outputs, which is also shown in Figs. 6(a) and 6(b).

The relationship between the output and the detuning at a fixed pump power is also plotted in Fig. 6(c). Due to the Kerr nonlinearity,

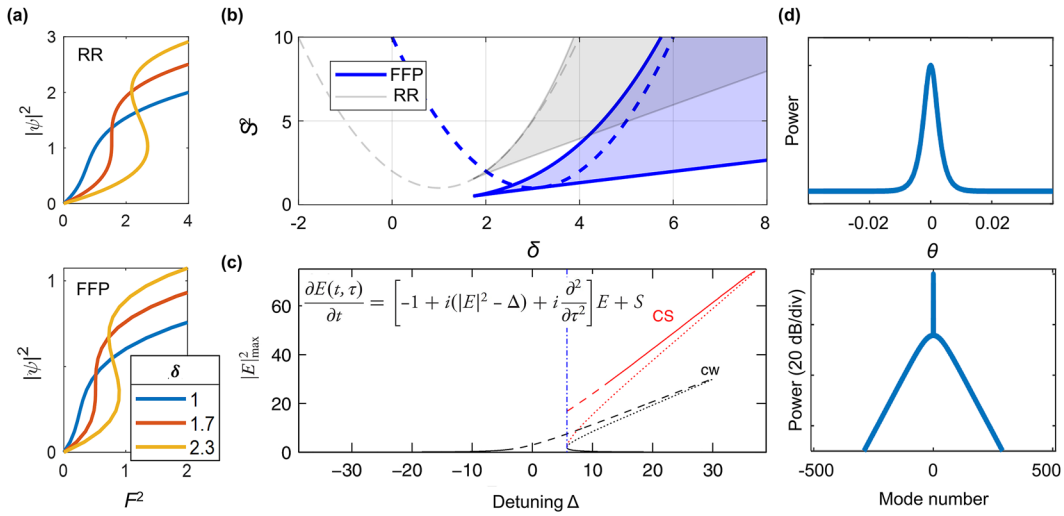

FIG. 6. Theoretical analysis based on normalized LLE for the case of anomalous dispersion. (a) Optical bistability for the ring resonators (RR) (top) and FP resonators (bottom); (b) bifurcation diagram showing the parameters leading to various stationary solutions; (c) output vs detuning. Solid curves, stable solutions; dotted curves, unstable solutions diverging to one of the other solutions; dashed lines, unstable solutions with more complex dynamics. Of note, this is obtained from another normalized form of LLE (in the inset). However, the conclusion that there is a good overlap between the DKS regime and the bistable regime still holds. (d) Temporal and spectral profiles of a single DKS. (c) Is adapted from Ref. 84.

the curve is tilted toward the red side. According to the linear stability analysis,[84,85] the middle branch is not accessible, while the upper branch is perturbation sensitive and modulationally unstable due to the interplay between Kerr nonlinearity and anomalous dispersion. Moreover, in the modulationally unstable regime for the homogeneous solution [Fig. 6(c)], a soliton solution can be found, as shown in Fig. 6(d). Therefore, it can be deduced that the soliton evolves from the modulation instability of the homogeneous solution, which is verified by the dynamics described in Sec. III B. Moreover, solitons exist only in the red-detuned regime ($\delta > 0$), so the phase shift coming from the nonlinear terms can be balanced by the phase rotation from the detuning term as well as the dispersion-related term.

B. Soliton dynamics

According to the bistability map in Fig. 6(c), the dynamics when the pump is scanned across the resonance from the blue-side [Figs. 7(a) and 7(b)] can be described using a phase diagram comprising continuous-wave, Turing pattern, chaotic combs, breathing soliton, and stable soliton regimes [Figs. 7(c) and 7(d)].

Turing patterns arise when the intracavity pump power exceeds the threshold of the optical parametric oscillator. A pair of symmetrical comb lines with respect to the pump is beneficial for squeezed light generation[86] due to the degenerate four-wave mixing process. In addition, the large frequency space of a comb pair is a good candidate as a low-noise terahertz wave source[87,88] through a large-bandwidth photodetector.

With the pump frequency close to the resonance peak, more comb lines arise from both degenerate and non-degenerate four-wave mixing processes, leading to non-phase-locked chaotic combs in the frequency domain and noise-like pulses in the time domain. The chaotic combs are useful in parallel LiDAR[89,90] to break the temporal and frequency congestion and achieve both millimeter-level ranging accuracy and millimeter-per-second-level velocity resolution. Besides, the chaotic combs have recently found application in high random number generation rates of 3.84 Tbps for a scalable decision-making accelerator.[91]

When the pump detuning reaches the edges of the soliton existing range, the noise-like pulses will be regulated into a breathing form with a smaller pulse number due to the interference with the pump laser and the interaction between pulses. The transition from chaotic combs to breathing solitons leads to a sudden drop in the intracavity average power, which may cause problems for soliton stabilization (see more details in Sec. III C). Additionally, breathing solitons are an interesting physical phenomenon, exhibiting intriguing dynamics like the Fermi–Pasta–Ulam recurrence between coupled modes in the frequency domain,[92] and might be a good optical platform for the study of time crystals.[93]

Finally, stable soliton can be achieved in the deep red-detuned regime, which is depicted as an up-tilted soliton step (see more details in Sec. III C). Of note, the final soliton number and their mutual phase relationships are random due to the stochastic transition from chaotic combs to breathing solitons. In addition, perturbation from other effects, such as the thermal effect,[37] avoided mode crossings,[94] dispersive wave emission, and the Raman effect,[95] can lead to a reduction of the soliton number, more soliton steps, and deterministic soliton number generation[94] during the scanning process.

C. Soliton properties

According to the coherent pumping scheme, the external CW pump is required for DKS sustainment, and the generated DKS

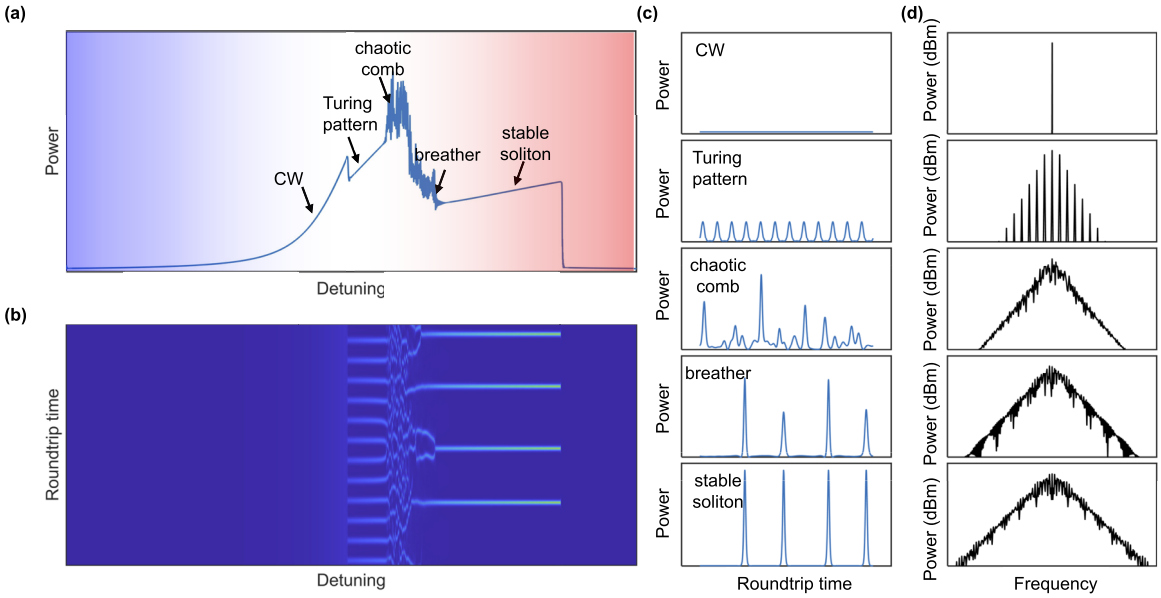

FIG. 7. Dynamics governed by the normalized LLE when pump frequency is scanned across the resonance from blue side to red side. (a) Intracavity average power vs detuning; (b) pulse evolution vs detuning; (c) temporal profiles; and (d) corresponding spectral profiles for the typical comb states. The roundtrip time determined by the reciprocal of the cavity FSR is usually tens of picoseconds (ps), much larger than the soliton pulse width of <1 ps.

always sits on a CW pedestal, which is verified by the pump comb line standing out above the soliton spectral envelope in Fig. 6(d). Therefore, the power conversion efficiency from the pump to DKS is usually as low as 1%.[96] Several schemes have been proposed to increase the power efficiency, including pulsed pumps,[96] dark soliton,[97] impedance matching using another coupled microresonator,[98] nonlinear coupling using quadratic nonlinearity,[99,100] and laser cavity soliton in microresonator-filtered lasers.[70,101]

The DKS power P_{sol} and pulse width $\Delta\tau$ are given by the following expressions:[39]

$$P_{sol} = \frac{2\eta A_{eff}}{n_2 Q_L}\sqrt{-2nc\beta_2\delta}, \tag{11}$$

$$\Delta\tau = \sqrt{-\frac{c\beta_2}{2n\delta}}, \tag{12}$$

where $\eta = Q_L/Q_{ext}$ characterizes loading efficiency from external coupling, Q_{ext} is the external or coupling Q factor, and Q_L is the loaded Q factor including both intrinsic loss and coupling loss, A_{eff} is the effective mode area, n_2 is the Kerr coefficient, and n is the refractive index. Hence, the soliton power and soliton pulse width are strongly dependent on the pump detuning δ, which is verified by the up-titled soliton step in Fig. 7(a).

Besides soliton power and pulse width, comb linewidth and soliton timing jitter are the other two important parameters for real-world applications. Usually, comb linewidth, which is the optical linewidth of comb teeth, is inherited from the pump laser through the four-wave mixing process.[102] Therefore, narrow comb linewidth requires a soliton pump laser with low frequency noise, which can be realized by an internally excited Brillouin laser (see Sec. IV C for details) or by self-injection locking the pump laser to the microresonator.[103] However, there exists a fundamental limit for the comb linewidth, which results from thermo-refractive noise due to the thermal fluctuation induced refractive index change. The thermodynamic fluctuations $S_{\delta T}(f)$ come from the general temperature variance given by[104]

$$\langle \delta T^2 \rangle = \frac{k_B T_{em}^2}{\rho_0 C V}, \tag{13}$$

where T_{em} is the temperature of the heat bath, k_B is the Boltzmann constant, ρ_0 is the density, C is the specific heat, and V is the mode volume. Of note, the temperature fluctuations $S_{\delta T}(f)$ can be numerically obtained by commercial software such as COMSOL Multiphysics for irregular geometries[105] or theoretically obtained for regular waveguides such as single-mode fiber.[106,107]

The relationship between frequency noise of the resonant frequency $S_\nu(f)$ and temperature fluctuations $S_{\delta T}(f)$ is given by[106,107]

$$S_\nu(f) = \left(\nu\frac{dn/dT}{n}\right)^2 S_{\delta T}(f), \tag{14}$$

where dn/dT is the thermo-optic coefficient and f is the offset frequency. Therefore, a large mode volume is beneficial for lower thermo-refractive noise but might come at the cost of an increased soliton pump threshold.

When a coherent soliton forms, the GVD induced FSR difference is compensated by the Kerr nonlinearity induced phase shift, leading to a narrowband beat note of comb spacings in the radiofrequency (RF) domain. The phase noise of the comb repetition rate and, equivalently the soliton timing jitter are the key parameters to characterize how equal the comb spacings are. According to Eqs. (11) and (12), pump detuning is one of the most important parameters affecting the soliton timing jitter through the detuning-dependent soliton peak power and the resulted change in nonlinear-phase shift from the Kerr effect. To reduce the detuning noise, the pump laser frequency should be tightly locked to the cavity, which can be accomplished by active locking methods such as the Pound–Drever–Hall (PDH) locking technique[108] or locking the soliton power to an ultralow-noise voltage reference.[109] Passive methods also exist, such as self-injection locking and Brillouin–Kerr soliton generation (see Sec. IV C for details). Compared to active methods, which are usually limited by the locking bandwidth, passive methods can achieve better noise performance, especially at high offset frequencies.

The soliton repetition rate can also be modified through the detuning-dependent Raman self-frequency shift and soliton recoil. Both effects can lead to an overall shift of the soliton center wavelength, leading to an inconsistency with the pump laser frequency. This shift induces a change in the group velocity, providing an additional channel to influence the repetition rate through the relation[110]

$$f_{rep} = \frac{1}{2\pi}\left[D_1 + \frac{D_2}{D_1}\Omega(\delta)\right], \tag{15}$$

where $\Omega(\delta)$ is the detuning-dependent shift of the soliton center frequency. The soliton Raman self-frequency shift is caused by intrapulse Raman scattering, where the blue spectral components serve as the pump and amplify the red spectral components, while the soliton recoil originates from a phase matching condition similar to Cherenkov radiation or dispersive wave emission.[111,112] Due to the soliton coupling to the dispersive wave, hysteretic behavior can be observed in both the dispersive-wave power and the soliton properties,[113] such as the soliton center frequency shift and the soliton repetition rate. In particular, the hysteresis behavior can reduce the soliton timing jitter at the quiet point,[113] wherein the coupling of pump frequency noise into the soliton repetition rate is greatly weakened. However, there is a limit to this noise suppression approach due to the frequency fluctuations of the dispersive wave, which are attributed to the intermodal thermal noise from imperfect mode overlap between the dispersive-wave mode and soliton-forming mode.[105]

There are fundamental limits for soliton timing jitter. The first one is the quantum noise limit due to the quantum noise seeded four-wave-mixing process, which is described by[114]

$$L_{\phi QN}(f) = \frac{\sqrt{2}\pi}{2}\sqrt{\frac{\Delta\nu}{\delta(-D_2)}}\frac{g}{\eta\Delta\nu^2}\times\left[\frac{1}{96}\frac{\Delta\nu(-D_2)}{\delta}\frac{\eta\Delta\nu^2}{f^2} + \frac{1}{24}\left(1+\frac{\pi^2 f^2}{\Delta\nu^2}\right)^{-1}\frac{\eta\Delta\nu^2}{\pi^2 f^2}\frac{\delta(-D_2)}{\Delta\nu}\right], \tag{16}$$

where $2\Delta\nu$ is the FWHM cavity linewidth, g is the frequency shift of a resonant mode per photon, and η is the quantum efficiency of the detector. According to Eq. (16), quantum noise can be reduced by a smaller GVD D_2 and a nonlinear frequency shift g ($g = \hbar\omega_0^2 c n_2 / V n^2$, where $\hbar$ is the Plank constant, ω_0 is the DKS center frequency).

Besides, the thermo-refractive noise (TRN) from thermal fluctuations will impose a noise limit on the repetition rate through two channels owing to the fluctuation of cavity resonance. First, TRN directly changes the resonator FSR, and the repetition rate fluctuation can be minified from TRN by a ratio between the soliton center frequency and the FSR. Second, the cavity resonance change will lead to detuning noise. For the repetition rate noise, the detuning noise limit from TRN is dominant at low offset frequencies (or at long time scales) and can be overcome by a strong active detuning control method, while the quantum limit is dominant at high offset frequencies (or at short time scales). According to Eqs. (13) and (16), a large mode volume is beneficial to lower both the quantum noise limit and the limits imposed by TRN. Therefore, a multimode fiber FP microresonator is a good candidate for both ultra-narrow comb linewidth and ultralow phase noise of the soliton repetition rate.

D. Solitons in FP resonators

There are several key differences between FP and ring resonators resulting from the two intracavity counterpropagating waves. The LLE for FP resonators (FP-LLE) is described as[115]

$$t_R \frac{\partial A}{\partial t} = -\left(\alpha + i\delta + i\frac{\beta_2 L}{2}\frac{\partial^2}{\partial \tau^2}\right)A + i\gamma L|A|^2 A + 2i\gamma L P_{cav} A + \sqrt{\kappa_{ex}} A_p, \tag{17}$$

where P_{cav} is the average power accumulated in the cavity, given by

$$P_{cav} = \frac{1}{t_R}\int_{-t_R/2}^{t_R/2} |A|^2 d\tau. \tag{18}$$

Similar to Eq. (9), the normalized form of FP-LLE is given by[116]

$$\frac{\partial \psi}{\partial t} = -\left(1 + i\delta + i\frac{\beta_2}{2}\frac{\partial^2}{\partial \theta^2}\right)\psi + i|\psi|^2\psi + 2i\left(|\psi|^2\right)\psi + S, \tag{19}$$

where $\langle|\psi|^2\rangle$ is the normalized average power accumulated in the cavity.

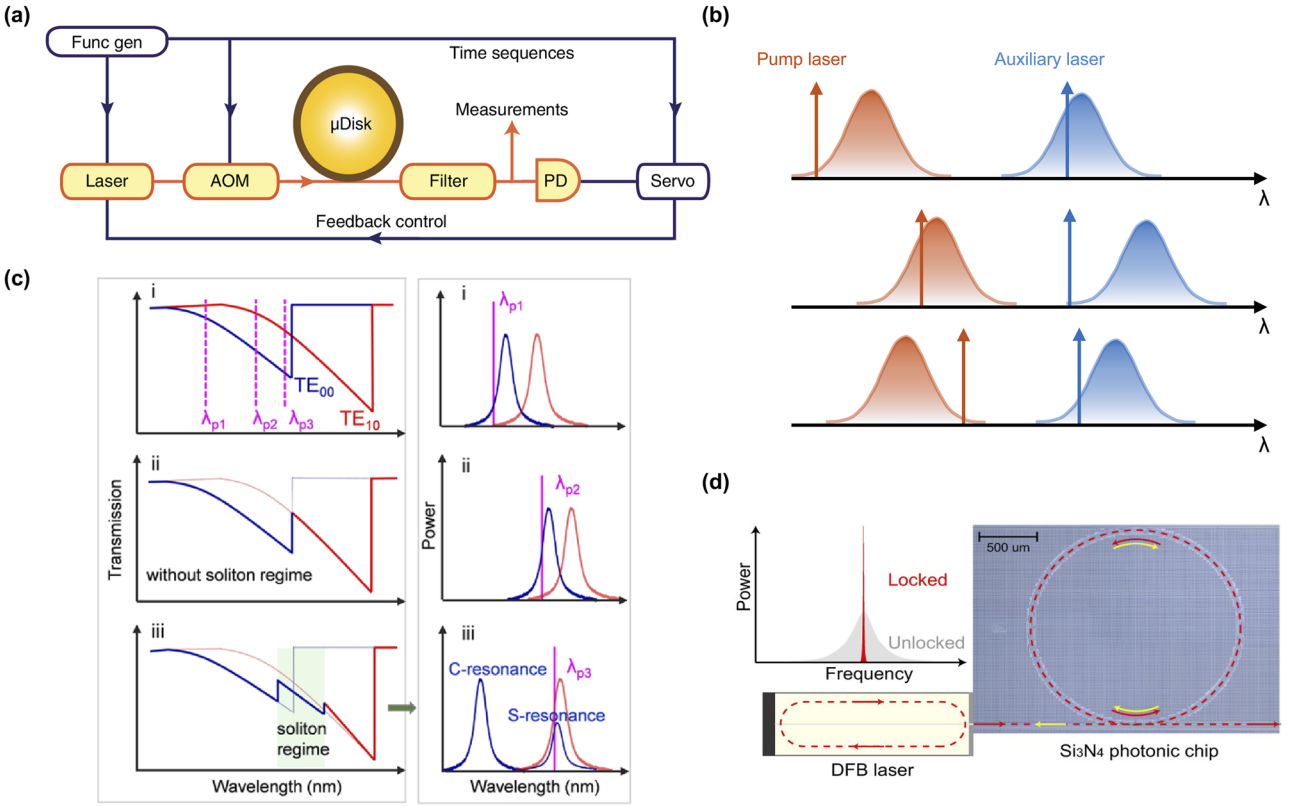

FIG. 8. Methods for soliton excitation and stabilization. (a) Using complex tuning schemes and active feedback loops. Func gen: function generator; AOM: acousto-optic modulator; μDisk: microdisk resonator; PD: photodetector. (b) Dynamics of soliton stabilization using an axillary laser. From top to bottom, the pump laser is scanned across the resonance from the blue side. When the pump is red-detuned and soliton is generated, the dropped intracavity power leads to the blue shift of the resonances. Such a blue shift will reload the auxillary laser into its resonance, prevent the power drop in the cavity and, therefore, stabilize the pump soliton at the red-detuning. λ: wavelength. (c) Dynamics of soliton stabilization by loading a single laser into two resonances (for different mode families) via avoided mode crossings. (d) Nonlinear self-injection locking method. Adapted from Refs. 109, 123, and 124.

Compared with the standard LLE for ring resonators, there is an additional nonlinear integral term representing phase modulation by twice the average intracavity power. This energy dependent detuning causes a cavity resonance frequency shift analogous to the thermal response, except instantaneously, due to the nature of the Kerr-nonlinearity. The theoretical comparison between ring-LLE and FP-LLE is shown in Figs. 6(a) and 6(b).[116] More analysis has shown that the coupling between detuning and the cavity's energy will cause a change in the soliton's existence range with either a continuous-wave or pulsed pump configuration.[116–118] Despite the differences, DKS dynamics and properties in FP resonators can be well understood from the results for ring resonators.

E. Soliton excitation and stabilization

Different from mode-locked lasers, DKS microcombs, either in ring resonators or FP resonators, usually cannot self-start and require excitation and stabilization techniques to achieve a stable microcomb for real-world applications. According to the analysis in Sec. III B, DKS is usually excited by scanning the pump frequency from blue detuning to red detuning, during which the modulation instability induced chaotic combs evolve into DKS combs at red detuning. However, the intracavity average power suddenly drops when solitons form [Fig. 7(a)], causing a blue shift of the cavity detuning due to the absorption-induced thermal nonlinearity in most microresonators. Therefore, the triggered DKSs, especially single solitons, are difficult to thermally stabilize even with a slow pump scanning speed.[119] Either complex tuning schemes and active feedback loops [Fig. 8(a)],[109] an additional auxiliary laser[120] [Fig. 8(b)] or avoided mode crossings [Fig. 8(c)] are required for eventually stabilized DKS, which prevents the minimization and integration of microcomb systems.

In order to remove the additional components, other methods utilizing passive effects in the microresonator are proposed for self-starting DKS microcombs. The first is the nonlinear self-injection locking (SIL) method [Fig. 8(d)].[121] The soliton is self-triggered by thermal nonlinearity and Kerr nonlinearity when the pump frequency is located on the red-detuned side. Since the SIL speed is much faster than the thermal effect, the triggered soliton can always stabilize itself. Despite the enabled turnkey operation of fully chip-based soliton microcombs, it requires deliberate debugging due to the small locking range, which strongly depends on both the frequency matching of the DFB-laser-microresonator pair and the environment-sensitive optical feedback phase. Moreover, the large soliton timing achieved jitter prohibits critical applications such as microwave photonics and timing distribution. The other methods utilize novel configurations of microresonator-filtered lasers,[70,101,122] where soliton self-excitation is achieved by the self-organized behavior in the laser and soliton self-stabilization is achieved by thermal nonlinearity compensation from either gain nonlinearity or a coexisting intracavity Brillouin laser. Details can be found in Sec. IV C.

IV. BRILLOUIN EFFECT ON SOLITON GENERATION

Various nonlinear effects can be utilized to enhance the microcomb performances, such as the Brillouin effect, the gain effect, and the Raman effect. Compared to microresonators based on planar waveguides, fiber microresonators have the unique advantage of including both the Brillouin effect and the gain effect. Therefore, we will focus on the fiber Kerr microcombs based on the Brillouin effect and gain effect in the next two sections. Readers can find more information on the Raman effect in microresonators in other papers, including the principle of Raman scattering,[125–127] Raman microlasers,[128–130] nonlinear competition between the Raman and Kerr effects[131–134] and Raman–Kerr soliton generation.[66,135–137]

A. Principle of backward and forward Brillouin scattering

Brillouin scattering is a third-order nonlinear effect where the polarization intensity depends cubically on the field. From the perspective of quantum mechanics, Brillouin scattering is recognized as an interaction between an input photon, a scattered photon, and an acoustic phonon inside the medium. The phonon comes from the lattice vibration, which can be caused by thermally induced Brownian motion or intense pump field induced electrostriction, corresponding to spontaneous Brillouin scattering or stimulated Brillouin scattering (SBS). When the phase matching condition (or the conservation of energy and momentum) is fulfilled, the photon-phonon interaction is maximized, and considerable conversion efficiency can be achieved. Brillouin scattering can also be explained from a macroscopic perspective. The accumulated displacement and vibration of the lattice result in an overall material strain (elongation) and change the refractive index through the photoelastic effect. Therefore, the periodically oscillating acoustic field causes a periodic refractive index change, creating an effective index grating that scatters the input light with a Brillouin frequency shift [Fig. 9(a)].

The energy or frequency of the scattered photon can be the difference or sum between the photon and the phonon, leading to Stokes wave or anti-Stokes wave generation. Both the Stokes and anti-Stokes shifted processes can be visualized as a "two-step" event (Fig. 10). The first step is the annihilation of an incident photon due to the simultaneous excitation of a lattice from the ground vibration state (or excited vibration state) to the intermediate state. In the second step, this lattice returns to the excited state (or the ground state) with the simultaneous creation of a scattered photon with a Stokes (or anti-Stokes) frequency shift. Following the Bose–Einstein distribution, the scattered strength of the anti-Stokes wave is usually weaker than the Stokes wave since the population in the ground vibration state is larger than that in the excited vibration state.

According to the relationship of propagation direction between the pump field and the scattered field, there are two kinds of Brillouin scattering: the forward and backward Brillouin scattering. For the backward SBS [Fig. 9(a)], the Brillouin frequency shift depends on the acoustic velocity, the refractive index, and the pump wavelength as $\Omega_B = 2\pi \cdot 2nv_s/\lambda$, which is usually around tens of GHz. The wavenumber of the generated hyper sound wave is at the same level as the optical wave [see the phase matching diagram in Fig. 11(a)]. The Brillouin gain bandwidth is usually tens of MHz, corresponding to a phonon lifetime of a few nanoseconds.

As for the forward SBS process, the acoustic modes no longer propagate along the light propagation direction but are guided in the transverse cross section [Fig. 9(b)], leading to near-zero wavenumbers [Fig. 11(b)]. The Brillouin frequency shift is determined by the transverse acoustic mode, which strongly depends on the material

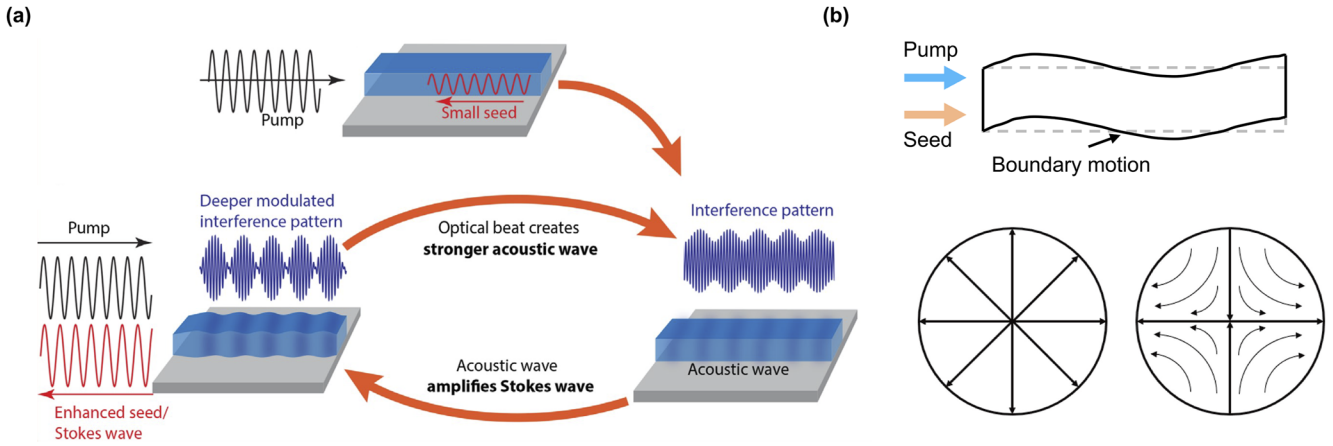

FIG. 9. Schematic of stimulated Brillouin scattering. For any type of stimulated scattering, there is a threshold requirement, i.e., the gain over unit propagation length should be greater than the losses due to various attenuation mechanisms. (a) Backward SBS:[138] the intense pump field and the small seed from an external laser or from quantum noise create an interference pattern and generate a pressure (or a force density) on the material, arising from radiation pressure or electrostriction. Such pressure excites an acoustic wave and, therefore, changes the dielectric properties as well as the medium's boundaries, effectively creating a grating that can scatter the pump light to the seed field if the phase matching condition is fulfilled. The Brillouin amplification process for the seed light in turn strengthens the interference pattern and leads to an exponentially increased Brillouin gain, which is a stimulated process. Therefore, backward Brillouin gain is near zero when the pump and seed are orthogonally polarized.[139] (b) Forward SBS: the gradient distribution of the intense pump field across the transverse directions can excite the acoustic wave with large transverse components through radiation pressure or electrostriction. Along the light propagation direction, the acoustic wave causes the boundary motion of the waveguide. The bottom figures show the two possible vibrational modes in fibers: radial acoustic mode (left bottom) and torsional-radial acoustic mode (right bottom). The radial acoustic mode causes only the phase modulation of the pump, while the torsional-radial acoustic mode causes both phase modulation and polarization modulation. Phase modulation can generate two sidebands (the Stokes and anti-Stokes lines), while polarization modulation can lead to polarization degradation. Adapted from Refs. 138 and 140.

and geometry. For example, in fibers, the acoustic wave is well confined in the cylindrical geometry [Fig. 9(b)] and, therefore, the phonon lifetime can reach the level of a few microseconds and lead to a Brillouin gain bandwidth of hundreds of kHz, which benefits optical information processing with high spectral resolution. In a multimode system, both backward and forward Brillouin scattering can occur between different spatial modes with considerable mode overlap, which is a promising method to avoid cascaded Brillouin processes (see details in Sec. IV B). The frequency shift of forward Brillouin scattering is usually around hundreds of MHz, which is smaller than tens of GHz for backward Brillouin scattering in fibers.

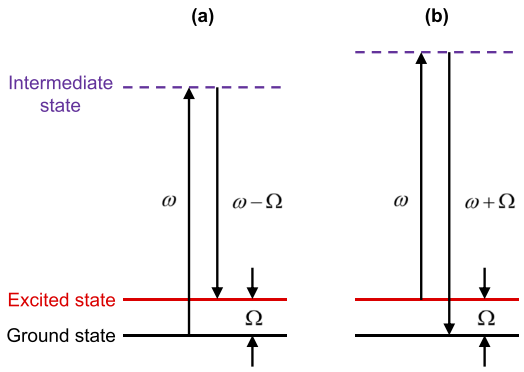

FIG. 10. Two kinds of Brillouin scattering processes illustrated by the two-step event. (a) Stokes shifted Brillouin scattering process; (b) anti-Stokes-shifted Brillouin scattering process.

Both the backward and forward Brillouin scattering can be realized between orthogonally polarized modes or different spatial modes in fibers, which are termed cross-polarized SBS or intermodal SBS. According to the principle in Fig. 9(a), there should be no cross-polarized gain due to no interference pattern between orthogonally polarized modes. For example, when the pump and probe are aligned to the fast and slow axes of a polarization-maintaining fiber, respectively, the measured cross-polarized SBS gain is near zero.[139] However, in optical fibers with weak and random birefringence, cross-polarized SBS gain is possible[139,141] despite lower gain compared to the SBS gain for the same polarizations. As for intermodal SBS, the imperfect mode overlap and induced lower SBS gain should be considered.

B. Stimulated Brillouin lasers in microresonators

In an oscillator, when the intracavity gain compensates for the loss, a coherent laser stands out from the noise. The gain can arise from the active gain such as pumped Erbium-doped fiber, or the nonlinear gain such as Brillouin gain, Raman gain, Kerr gain and quadratic nonlinearity induced parametric gain.

To generate low-threshold stimulated Brillouin lasers (SBL), the Stokes mode resonance should have a good overlap with the Brillouin gain spectrum (Fig. 12). If the Stokes mode resonance peak aligns with the Brillouin gain spectrum peak, which means a perfect phase matching condition (when pump detuning is zero), then the Brillouin laser threshold is described as below:[142]

$$P_{th} = \frac{1}{\Lambda}\frac{\pi^2 n^2}{g_B Q_P Q_S}\frac{V}{\lambda_P \lambda_S}, \tag{20}$$

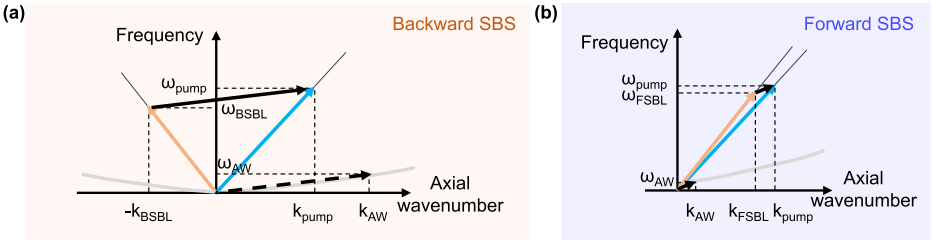

FIG. 11. Phase matching diagram. (a) Backward SBS; (b) forward SBS. Adapted from Ref. 140.

where Λ is the spatial overlap factor between the pump mode (P) and Stokes mode (S) and g_B is the Brillouin gain coefficient, which is defined as

$$g_B = \frac{\gamma_e^2 \omega_0^2}{2\pi n v_s \rho_0 \Gamma_B}, \tag{21}$$

where γ_e is the electrostrictive constant, v_s is the speed of sound, and Γ_B is the loss rate of the density wave. The frequency shift between the Stokes mode resonance peak and the Brillouin gain spectrum will lead to an increased SBL threshold, non-zero SBL detuning, and degraded SBL linewidth, which will be discussed later.

Different ways have been proposed to achieve better alignment between the Stokes mode resonance and the Brillouin gain spectrum, depending on the characteristics of both modes. If the Stokes mode shares the same mode family with the pump, which is the intramodal SBS case, the cavity length should be carefully adjusted within only a few millimeters[143] to ensure the Brillouin frequency shift is an integer multiple of the free spectral range (FSR) since Brillouin gain bandwidth is usually tens of MHz. Therefore, fine cavity length fabrication is one of the key challenges preventing efficient SBL generation in microresonators. Another method is the so-called intermodal SBS, which utilizes different mode families, such as cross-polarized modes, different spatial modes, or a combination. In an FP microresonator made from highly multimode fiber by our group,[54] it is quite easy to achieve efficient intermodal SBL generation regardless of the cavity length. Of note, the intramodal SBL generation usually leads to cascaded high-order SBL generation, which limits the power scaling of the first-order SBL. A large group velocity difference induced by a large Brillouin frequency shift and/or a large GVD, such as in diamond,[144] is required to increase the threshold of the cascaded SBL generation. As for the on-chip microresonators, the engineering of the avoided mode crossing can increase the loss of the cascaded Brillouin mode resonance and thus increase the threshold of high-order SBL.[145] Besides, the gratings on the waveguide or microresonator can inhibit the cascaded SBS.[146,147] Compared to the intramodal method, intermodal SBL generation is more general and efficient for cascading inhibition and SBL power scaling. Of note, the aforementioned two methods can be applied to both backward and forward Brillouin laser generation.

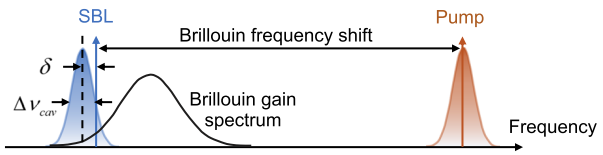

FIG. 12. Illustration of SBL phase mismatch. The lasing SBL deviates from its resonance peak due to the mode pulling effect, which can maximize the SBL output power through maximized overlap between the Brillouin resonance and Brillouin gain spectrum.

The dynamics of backward SBL generation can be modeled by the three-wave (two optical waves and an acoustic wave) coupled equations[148]

$$\begin{aligned}
\frac{\partial A_F}{\partial t} &= \frac{A_F}{2\tau_F} - i\frac{\gamma_e \omega_F}{4n^2\rho_0}\rho A_B \Lambda_F - i\delta_F A_F + \sqrt{\frac{1}{\tau_{ext}}}S, \\
\frac{\partial A_B}{\partial t} &= \frac{A_B}{2\tau_B} - i\frac{\gamma_e \omega_B}{4n^2\rho_0}\rho^* A_F \Lambda_B - i\delta_B A_B, \\
\frac{\partial \rho}{\partial t} &= i\frac{\Omega_B^2 - \Omega^2}{2\Omega}\rho - \frac{\Gamma_b}{2}\rho - i\frac{\varepsilon_0 \gamma_e}{4\Omega}\frac{\ell_\rho^2}{R^2} A_F A_B^* \Lambda_\rho - i\delta_\rho \rho,
\end{aligned} \tag{22}$$

where A_F, A_B, and ρ are the forward (pump), backward (SBL), and acoustic wave, respectively; δ_F, δ_B, and δ_ρ are the detunings of pump, SBL, and acoustic fields with respect to their corresponding resonances; Λ_F, Λ_B, and Λ_ρ are the mode overlaps of the forward, backward, and density waves; τ_F and τ_B are the lifetimes for the forward and backward waves; $1/\tau_{ext}$ is the external coupling rate of the pump; Γ_B is the loss rate of the density wave (Brillouin gain bandwidth); Ω_B is the Brillouin frequency shift; and Ω is the actual frequency shift between the pump frequency and the generated SBL frequency.

According to Ref. 148, the detuning relationship between the pump field and the SBL is given by[148]

$$\delta_B = \frac{\delta_F - \left[\left(\Omega_B^2 - \Omega^2\right)/2\Omega\right]}{1 + \Gamma_B \tau_B}. \tag{23}$$

Therefore, the detuning of the backward SBL is modulated by $1/(1+\Gamma_B\tau_B)$ times the pump detuning. For example, in a high-Q microresonator, the product of the Brillouin gain bandwidth and cavity photon lifetime is larger than 10, which means SBL detuning noise can be suppressed by more than 10 dB. This advantage can be utilized for generating solitons with ultralow-jitter since the soliton's features are strongly detuning-dependent, which is discussed in Sec. III C.

Apart from detuning noise suppression, SBL frequency noise can also be effectively reduced by a narrowing factor $(1+\Gamma_B\tau_B)^2$[62,149] at the perfect phase matching condition. This noise suppression is achieved by the quick dampening of the pump noise

through the acoustic wave because the phonon decay rate (Γ_B) is much faster than the intracavity photon decay rate ($1/\tau_B$). The latest SBL fundamental linewidth is 53 mHz,[54] which was achieved in 2022 by our group in a multimode fiber FP microresonator with Q factors of 384×10^6.

On the other hand, the shift between the Stokes mode resonance peak and the Brillouin gain spectrum peak can lead to a reduction of the narrowing factor[150] due to the increased amplitude-to-phase noise coupling at the imperfect phase matching condition (deviating from the maximum SBS gain). In this case, the SBL linewidth is given by

$$\Delta\nu_{SBL} = \Delta\nu_0\left(1 + \zeta^2\right), \tag{24}$$

where $\Delta\nu_0$ denotes the non-broadened SBL linewidth and $\zeta = 2\delta/\Delta\nu_{cav}$ determines the linewidth broadening factor (see Fig. 12).

Phonon noise can be squeezed if the phonon decay rate is slower than the intracavity photon decay rate, which can be realized by utilizing a guided acoustic wave in the forward Brillouin scattering process, such as in microresonators made from fibers or suspended waveguides. For example, in an on-chip silicon microresonator,[151] the guided acoustic wave results in a longer phonon lifetime than the intracavity photon lifetime. Therefore, pump noise is directly damped to the generated forward SBL. A noise-suppressed phonon can be deduced from a noise-suppressed electrical beating signal between the two correlated optical fields. Recently, the first 20-dB noise-squeezed forward SBL has been achieved by our group by utilizing a short-lifetime phonon mode in a multimode fiber FP microresonator,[140] reaching the noise level of backward SBL. Of note, the dynamics of forward SBL generation in microresonators can be similarly modeled by the three-wave coupled equations as in Eq. (22).

C. Kerr soliton generation with backward Brillouin effect

The SBS effect can cooperate with other intracavity nonlinear effects, which provides opportunities to improve noise performance and benefits more applications that require ultrahigh laser coherence. The cascading between the Brillouin and Kerr effects dates back to 2009[62] when Brillouin-enhanced Kerr combs were demonstrated in a monolithic highly nonlinear fiber cavity. After that, it is found that the interaction between the Brillouin and Kerr effects in a chalcogenide fiber resonator[152,153] and later in an on-chip FP resonator[146,154] can lead to phase locked frequency combs. Recently, our group showed for the first time that the controlled interaction between SBS and Kerr nonlinearity can result in two advantages of the generated SBL DKS: self-stabilization without active feedback control and ultralow noise, including ultra-narrow comb linewidth and ultralow DKS timing jitter.[63] These demonstrations were first performed in a monolithic highly nonlinear fiber Fabry–Perot (HNLF FP) resonator[63] and later extended to graded index multimode fiber Fabry–Perot (GRIN-MMF FP) resonators[54] and other DKS platforms such as silica microdisk resonators,[150] silica wedge resonators,[155] and silica microspheres[40] by other groups. In our original experiment, we introduced a novel two-step pumping scheme where the primary pump at one mode family

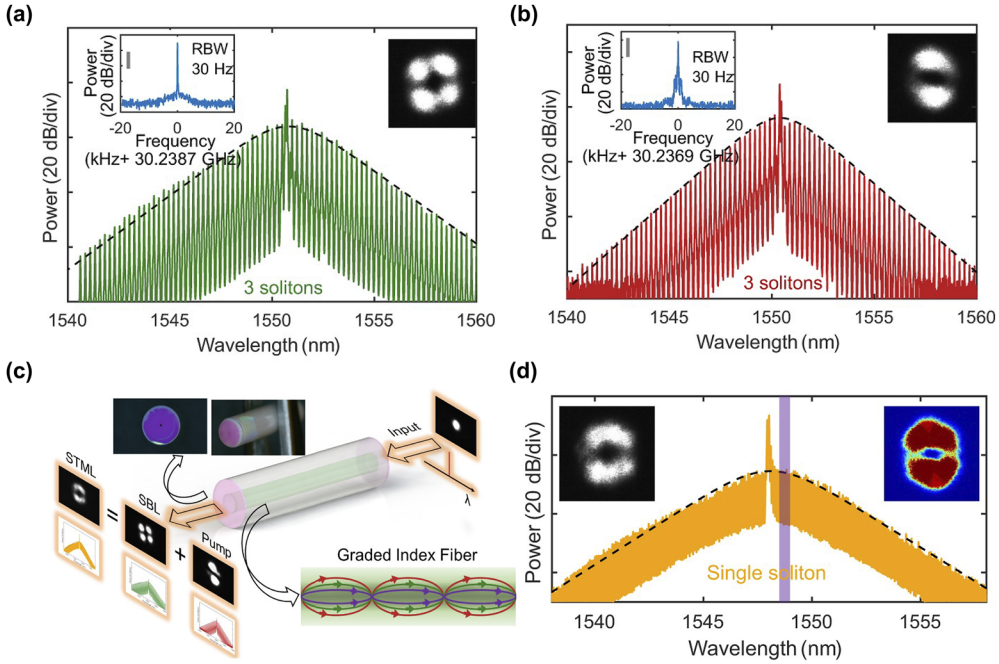

FIG. 13. Soliton generation utilizing two-step pumping scheme in a fiber FP microresonator with an FSR of ~10 GHz. Insets are the soliton spatial mode: (a) SBL soliton generation; (b) pump soliton generation; (c) schematic of spatiotemporally mode-locked DKS in a graded index fiber FP microresonator; (d) spatiotemporal mode-locked soliton generation. The mode profile is the superposition of both pump mode and SBL mode. Adapted from Ref. 54.

triggers SBS lasing that served as the secondary pump for DKS generation at another mode family. The blue-detuned primary pump and the red-detuned SBL can work together to compensate for the detrimental cavity thermal nonlinearity that limits the reliability and robustness of SBL DKS generation [Fig. 13(a)], with the same principle used in the auxiliary-assisted soliton generation method,[120,156] which is discussed in Sec. III E [Fig. 8(b)]. In principle, by adjusting the relative magnitude between the pump-Brillouin resonance offset frequency and the Brillouin frequency shift, either an SBL comb or a pump comb can be generated. In

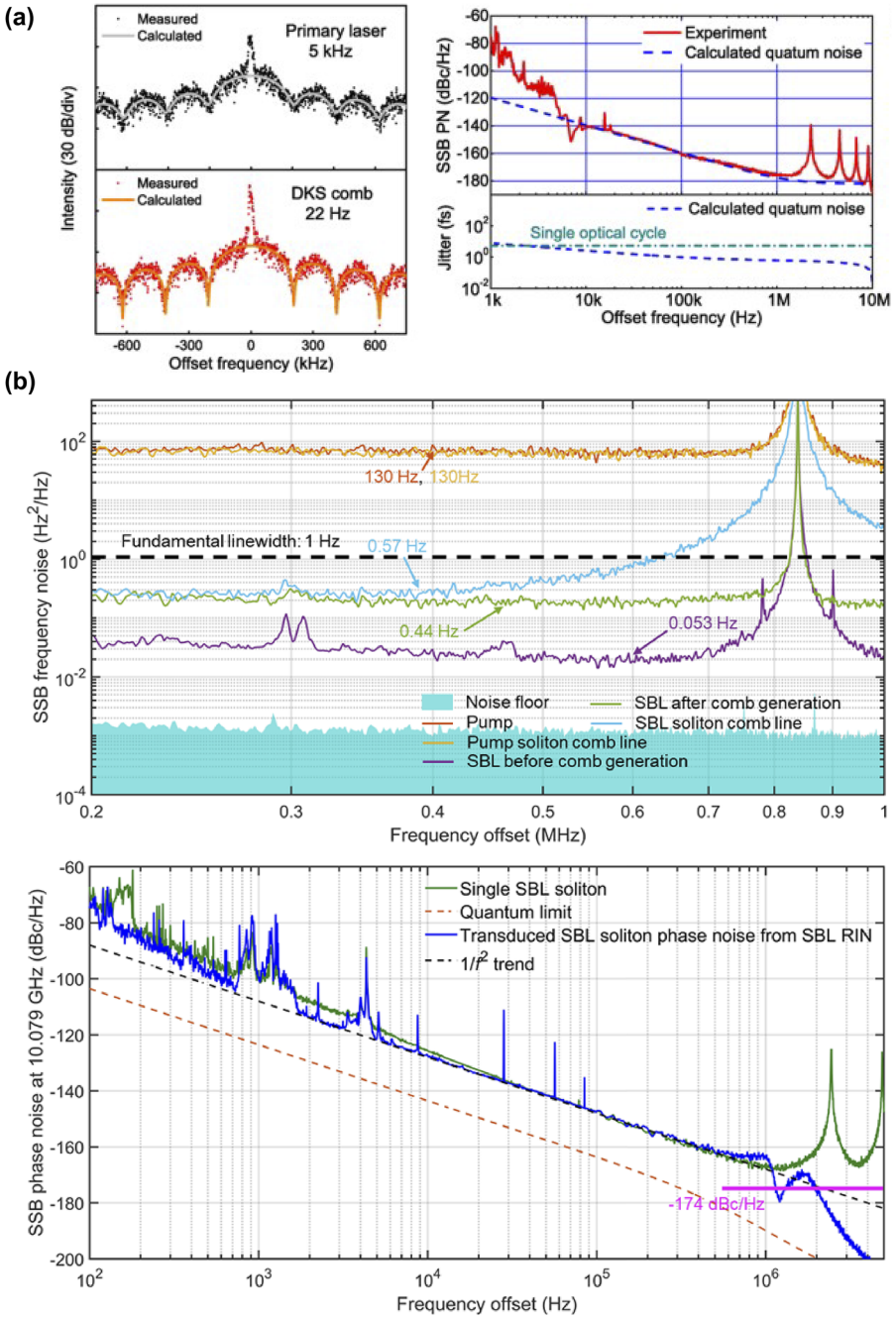

FIG. 14. Characteristics of the Brillouin–Kerr comb including microcomb linewidth and DKS timing jitter. (a) SBS between two modes with orthogonal polarizations in a monolithic fiber FP resonator; (b) SBS between two spatial modes in a monolithic fiber FP microresonator. Adapted from Refs. 54 and 63.

the experiment, we conveniently tuned the fiber stress, thus the Brillouin frequency shift, and realized DKS generation in the pump mode family [Fig. 13(b)] with a red-detuned pump and a blue-detuned SBL. Moreover, the two-step pumping scheme provides a feasible route toward high-dimensional nonlinear cavity dynamics such as dual comb or multiple comb generation using only a single pump! For instance, our group recently demonstrated the generation of spatiotemporal mode-locked (STML) DKS [Figs. 13(c) and 13(d)] for the first time in the GRIN-MMF FP microresonator with low modal dispersion enhanced intermodal nonlinear interaction,[54] while the Yao group has achieved repetition-rate locked cross-polarized solitons in a monolithic highly nonlinear fiber FP resonator.[64] Our group and the Yao group have also shown the feasibility of multiple DKS microcomb generation by high-order intermodal SBLs.[40,140,157]

The two-step pumping scheme also takes advantage of noise suppression in the SBS process, as mentioned earlier in Sec. IV B, including comb linewidth narrowing and detuning noise suppression. Due to the degenerate four-wave-mixing process, the DKS comb linewidth is the same as the pump linewidth[102] if other nonlinear effects are not considered.[158] Therefore, soliton microcombs pumped by the intracavity SBL act as multiple single-frequency lasers with ultra-narrow linewidth. Besides this, SBL detuning noise suppression leads to large SBL soliton jitter reductions. In the first demonstration in an HNLF FP resonator, a microcomb linewidth of 22 Hz and quantum-limited DKS timing jitter of 995 attoseconds for averaging times up to 10 μs were achieved [Fig. 14(a)].[63] Such ultralow timing jitter can be measured by an all-fiber reference-free Michelson interferometer (ARMI) timing jitter measurement apparatus as described in Refs. 159 and 160. By implementing the two-step pumping scheme between two spatial modes in a GRIN-MMF FP resonator, our group recently demonstrated unprecedented microcomb linewidth of 400 mHz and DKS timing jitter of 500 attoseconds for averaging times up to 25 μs [Fig. 14(b)].[54] The enhanced performances were attributed to the improved Q factor, lower thermo-refractive noise,[104] and lower quantum limit[114] of the GRIN-MMF FP resonator.

Of note, all the reported SBL DKS generation utilizing the two-step pumping scheme is realized by intermodal SBS and/or cross-polarized SBS. In theory, the intramodal SBL DKS is also feasible with avoided cascaded SBL and high-power first-order SBL generation. Moreover, our proposed two-step pumping scheme should also be applicable to Raman–Kerr soliton generation in crystalline microresonators with narrowband Raman gain such as AlN microresonators,[161] as well as the forward-Brillouin–Kerr soliton generation. Besides, the two-step pumping scheme can also be applied for Kerr soliton generation from either the forward SBL or the second harmonic field.

D. Forward Brillouin scattering effect on DKS

Forward Brillouin scattering, also referred to as guided acoustic wave Brillouin scattering, was first studied by Shelby *et al.* in single-mode fibers[162,163] due to the good acoustic waveguide enabled

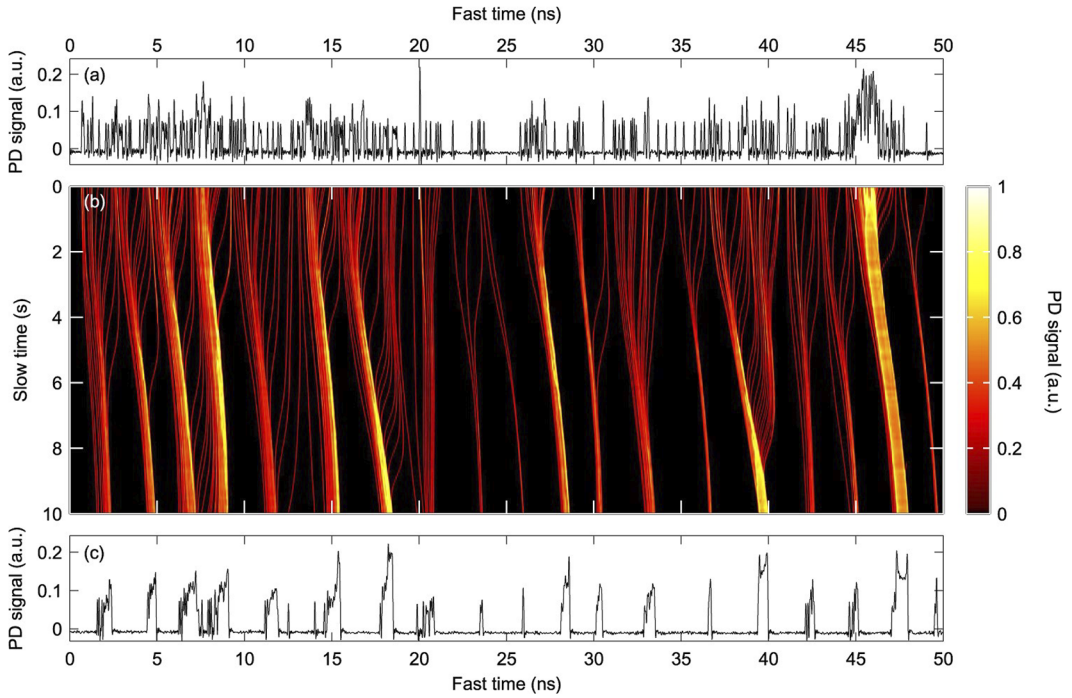

FIG. 15. Bunching of temporal cavity solitons via forward Brillouin scattering. (a) and (c) Temporal intensity profiles of the intracavity field measured (a) right after exciting temporal CSs and (c) after those CSs have freely interacted for 10 s. (b) Density plot corresponding to a vertical concatenation of such profiles measured at regular intervals and revealing how the field dynamically evolves over time (top to bottom). The top and bottom lines correspond to the profiles shown in (a) and (c), respectively. PD: photodiode. Adapted from Ref. 166.

by the cylinder geometry [Fig. 9(b)]. The forward Brillouin scattering has been discovered to impose long-range conservative soliton interaction since 1989.[164] In 2013, Jang *et al.* observed pairs of DKSs interacting over a range as large as 8000 times their width in a long passive fiber cavity.[165] The interactions are so weak that, at the speed of light, an effective propagation distance on the order of an astronomical unit can be required to reveal the full dynamical evolution. The interactions are mediated by transverse acoustic waves generated in the optical fiber by the propagating solitons through electrostriction. First, the leading DKS excites the transverse vibration and acoustic waves through forward Brillouin scattering. Second, the acoustic wave is guided and reflected back-and-forth from the fiber cladding–coating boundary back into the fiber core, generating echoes with a period determined by the cladding diameter and the acoustic speed. Third, the trailing cavity soliton sees the refractive index change caused by the acoustic wave through electrostriction, resulting in the interaction between two solitons.

By exciting a large number of DKSs with random temporal separations in a continuously driven passive fiber resonator, the same group observed the real-time dynamics of DKS bunching from random sequence into regularly spaced aggregates (soliton crystal)[166] (Fig. 15), where the acoustic wave played the key role. Therefore, it is quite possible that the forward SBS can impose additional noise on the soliton jitter and comb linewidth for the fiber microcombs, although it has not been well studied.[167]

Besides these interesting optoacoustic phenomena, solitons in fiber resonators with active gain can be flexibly manipulated by enhancing optoacoustic interaction in photonic crystal fibers, where both the optical and acoustic fields are tightly guided in a small area.[168] Interesting phenomena such as the formation and dissociation of optical supramolecular structures[169] and novel laser sources such as GHz-repetition-rate mode-locked fiber lasers[170] have also been demonstrated.

V. GAIN EFFECT ON SOLITON GENERATION

To apply optical frequency combs for extensive real-world applications, three trends have arisen to push the comb repetition rate into microwave rates. The first is to shrink the size of the mode-locked laser, which is mainly limited by the requirement of high gain and a reliable saturate absorber. The second is to increase the size of the DKS comb in a microresonator, which is mainly limited by propagation loss and an increased pump threshold. The last is to combine the mode-locked laser and DKS in a novel configuration termed a microresonator-filtered laser, which will be discussed in detail later.

A. Passively mode-locked monolithic fiber lasers

Besides the Kerr-lens mode-locked solid-state laser,[171] harmonic mode locking,[172] active mode-locking,[173] and optoacoustic mode-locking,[170] monolithic fiber FP lasers mode-locked by material-based saturable absorbers are another alternative to generate robust pulses at >5 GHz repetition rates with low cost and compact size. The keys to low-threshold mode-locking are the low-energy saturable absorbers and high gain (or low loss), which require low-transmission of the FP cavity coating, highly doped gain fiber, and relatively large pump power in a centimeter-long fiber. The demonstrations of mode-locked fiber FP lasers were first performed to achieve a 5-GHz pulse train by carbon nanotubes[174] and later extended to realize a pulse repetition rate of 17.2 GHz.[175] Other saturable absorbers such as graphene [Fig. 16(a)][176,177] and semiconductor saturable-absorber mirror (SESAM)[178–180] are introduced to achieve mode-locked pulses with electrical tunability [Fig. 16(b)],[177] high stability, and wavelength extension.[180] Despite the remarkable results, more studies are necessary to increase the comb bandwidth and lower the pulse timing jitter for practical applications.

B. Externally driven DKS generation with active gain

Active gain material can be incorporated to increase the Q factor and lower the pump threshold for DKS generation. Of note, these microresonators without saturable absorbers are configured to have a gain close to the lasing threshold, which is fundamentally different from mode-locked lasers. Such configuration ensures that DKS generation is still in the conventional framework where DKS is coherently driven by the external CW pump.

The first demonstration is performed in a long class B Erbium-doped fiber cavity,[181] showing that spontaneous soliton formation is forbidden with a CW external pump but becomes accessible with a pulsed external pump depending on the gain saturation. In the regime of strong gain saturation under continuous-wave driving, the linear stability analysis shows (i) modulation instability of the homogeneous states does not exist; (ii) soliton exists in a large range of detunings. The soliton branch is very different from that of conven-

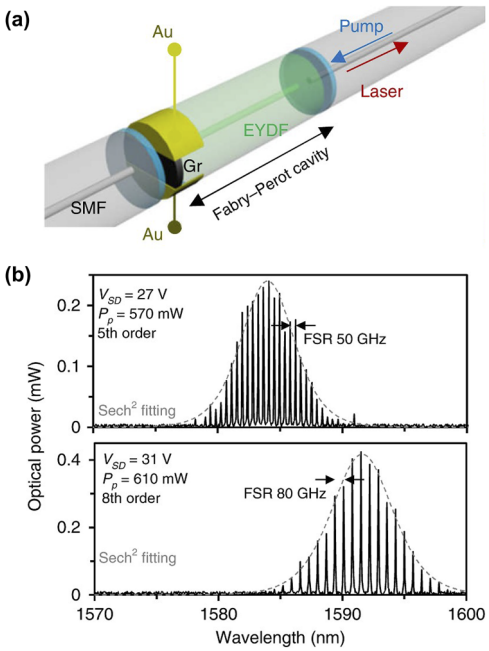

FIG. 16. Electrically controllable laser frequency combs in graphene-fiber microresonators.[157] (a) Architecture of the implementation. The graphene heterostructure is incorporated on one side of the fiber FP microresonator. (b) Electrically controllable harmonic-mode locking with repetition rates of 50 and 80 GHz. Adapted from Ref. 177.

tional DKS emerging from a homogeneous saddle-node bifurcation, as shown in Fig. 6(a). Since the spontaneous formation of solitons is prohibited due to the lack of MI, solitons can be observed by injecting a seed pulse. In the regime of weak gain saturation, the linear stability is similar to the conventional DKS, as in Sec. III A. This can be qualitatively understood with the modified LLE, where the loss term is compensated by a linear small-signal gain. The most significant finding is that, to the limit of the equipment, the so-called active cavity soliton does not suffer from the Gordon–Haus jitter resulting from the amplified spontaneous emission.

Another example is the gain-assisted chiral soliton microcombs in Er-doped microspheres.[182] Two counterpropagating solitons with different repetition rates, which are assisted by backscattering and active gain, are demonstrated with a unidirectional continuous pump.

Recently, it was shown that a generalized LLE can also be used to describe the dynamics of a class B quantum cascade laser (QCL) with an external pump under weak saturation.[183] Therefore, localized structures such as the Turing pattern and DKS in externally pumped QCL were predicted and numerically analyzed.[183,184] Surprisingly, the first DKS generation in QCL was demonstrated without an external pump.[185] Although not fully understood, the following three conditions might be the key conditions for QCL soliton generation: (i) a ring structure that removes instantaneous gain

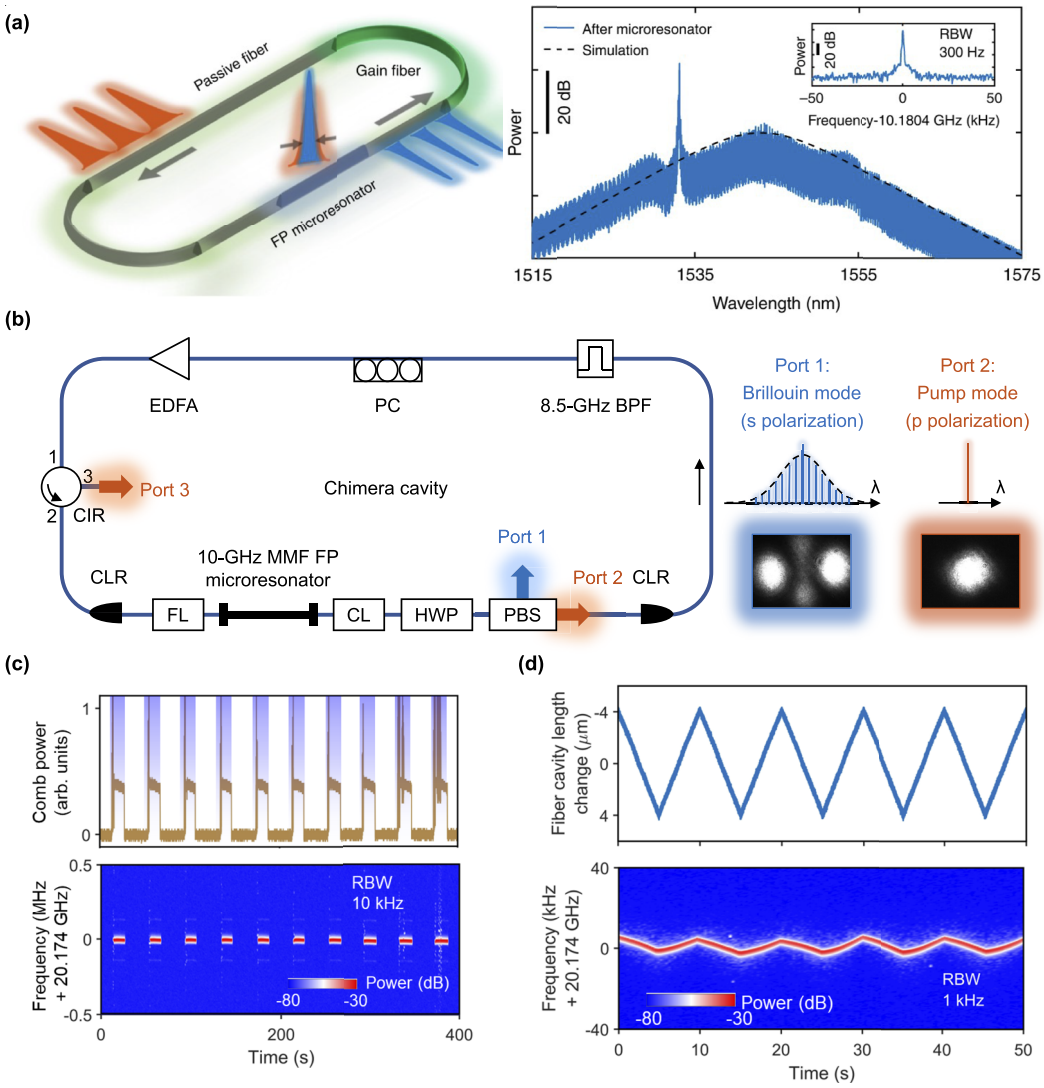

FIG. 17. DKS microcomb generation in a microresonator-filtered fiber laser. (a) Laser cavity soliton with broadband intracavity filter; (b) Turkey soliton with narrowband intracavity filter. EDFA: Erbium-doped fiber amplifier, CIR: circulator, CLR: collimator, FL: focusing lens, CL: collimating lens, HWP: half-wave plate, PBS: polarization beam splitter, BPF: band-pass filter, PC: polarization controller. Single frequency lasers in the large fiber cavity for the pump, while in the microresonator, the pump generated SBL excites the soliton microcomb. (c) Turnkey test by modulating the 980-nm pump power. (d) Modulation of soliton repetition rate by changing the large fiber cavity length. Adapted from Refs. 70 and 122.

grating; (ii) unidirectional operation that minimizes optical backscattering through spontaneous symmetry breaking; and (iii) anomalous dispersion. Additionally, gain saturation may also be a reason why the results are different from previous theoretical analyses.[186] Excitingly, without an external pump, higher soliton efficiency can be achieved, and it is more straightforward to extend the DKS wavelength range to the mid-infrared and terahertz regimes. Despite the remarkable results, more studies are necessary to better understand its physical mechanism, how it differs from saturable absorber enabled mode-locking, and what the consequences are.

C. DKS microcomb generation in a microresonator-filtered fiber laser

The configuration of a microresonator-filtered fiber laser, where a microresonator is nested into a fiber laser cavity [Fig. 17(a)], is a novel configuration that combines the advantages of fiber lasers enabled self-starting and microresonators induced ultrahigh pulse repetition rate. In this configuration, the microresonator plays two roles: (i) a periodic intracavity filter and (ii) the nonlinear Kerr medium.[70] The final lasing modes are the common modes of both the microresonator and the laser cavity. Similar to the self-injection locking method,[187–190] such a configuration provides another method for locking the lasing mode to the microresonator resonance as well as narrowing the optical linewidth determined by the microresonator Q factor[189] since only a high-coherent laser can circulate in the cavity.

Usually, this configuration requires an intracavity filter inside the fiber laser cavity to select the desired wavelengths, as well as a delay line to fine tune the relative position of lasing modes with respect to the microresonator's resonance. With a broadband intracavity filter, multiple common modes can lase and experience amplification in the active fiber. When the lasing modes are blue detuned with respect to the microresonator's resonance,[101] phase locking can be achieved through the dissipative four-wave-mixing process and form a coherent localized Turing pattern.[191]

Additionally, the so-called laser cavity soliton (LCS)[101] can be achieved by fine tuning the delay line. According to our recent study,[70] for LCS, the red-detuned nested microresonator has a nonlinear transmission that provides an effective saturable absorber to mode lock the fiber laser. The insight leads to the prediction of a new class of bright chirped LCS and the demonstration of a mode efficiency as high as 90.7%, approaching the theoretical limit of 96%. In addition, intriguing LCS interaction phenomena, including optical Newton's cradle, were experimentally observed.[70] Besides the free background and high mode efficiency, LCS is also found to be self-starting, which is attributed to the balance between thermal nonlinearity in the microresonator and gain nonlinearity in the fiber laser.[192]

To improve the noise performance and long-term stability of microcombs for practical applications, our group recently introduced a novel two-step pumping scheme (Sec. IV C) in the microresonator-filtered laser configuration [Fig. 17(b)] and realized decoupling between the pump generation and the comb generation.[122] Only a single-frequency laser is circulating in the large fiber laser cavity resulting from the narrowband filter, while the microcomb generation is realized by the pump-generated cross-polarized and intermodal SBL within the microresonator. Our approach for self-starting solitons [Fig. 17(c)] does not suffer from the vulnerability to feedback phase fluctuation[121] and enables the deterministic selection of DKS soliton numbers. In addition, we demonstrate the self-healing capability of returning to the original comb state from instantaneous perturbations, excellent long-term stability, and modulation capability [Fig. 17(d)]. More importantly, our approach allows access to ultralow noise comb states. The turnkey Brillouin-DKS frequency comb achieves a fundamental comb linewidth of 100 mHz and a DKS timing jitter of 1 fs for averaging times up to 56 μs. We claim that our approach (patent pending) is a universal topology for turnkey DKS generation and has the potential for fully on-chip integration. Moreover, SBS is not the only intracavity effect that can be used to decouple the pump and comb generation. Avoided mode crossing[123,193,194] can also be utilized, and it relaxes the need to match the microresonator FSR with the Brillouin frequency shift, rendering AMX more flexible and user-friendly for mass production of user-friendly and field-deployable comb devices.

VI. SUMMARY AND OUTLOOK

The fiber FP microresonator is an incredibly promising platform with boundless potential, waiting to be harnessed. This platform can leverage well-established fiber optics, which has been a cornerstone of modern optics since its inception in 1970. Researchers have explored the advantages of ultralow loss (<0.3 dB/km), large mode areas, and spatiotemporal mode-locking. The achievement of ultrahigh-Q microresonators (>10^9) with a large mode volume has enabled the development of novel comb sources with significantly improved performance, including ultranarrow comb linewidth and minimal soliton jitter for applications with ultralow noise requirements, such as optical clockworks and optical synthesizers. Furthermore, fiber FP microresonators hold the potential to address practical challenges in microcomb utilization, including self-starting functionality and high-power efficiency with a continuous-wave pump. For instance, our group has demonstrated self-starting microcombs with high efficiency in a fiber laser nested with a fiber FP microresonator (see Fig. 17).

Beyond the examples discussed, numerous other exciting and innovative directions are anticipated. First, there is the potential for extending the wavelength range of microcombs in fiber FP resonators. For instance, it is feasible to generate mid-infrared microcombs using chalcogenide fibers through sophisticated dispersion engineering, while visible microcombs can be produced in periodically poled fibers[195] via cascaded second-order nonlinearities.[79,80,196] Second, the development of all-fiber integrated microcomb systems is worth exploring. For example, further integration of the fiber FP microresonator filtered lasers (Fig. 17) can enhance the applicability of comb-based technologies in the field. Furthermore, all-fiber integrated systems compatible with other fiber-based technologies can minimize coupling losses, which is crucial for applications like squeezed light generation.[86] The third avenue of investigation involves exploring additional degrees of freedom offered by fibers, such as spatial modes and chiral modes. This exploration is likely to lead to a plethora of high-dimensional phenomena and applications, for example, optical vortex Brillouin lasers,[197] temporal solitons with optical vortex in fiber,[198] mode division multiplexing for optical communications, multi-core fibers for multiple combs,[199] and so

on. Additionally, ultrahigh-Q fiber microresonators can serve as a test bed for exploring interdisciplinary effects, such as integrating 2D materials for lab-on-fiber technology[200,201] and optical sensing applications.

Despite these fascinating prospects, numerous challenges remain. The first challenge involves increasing the Q factor of fiber FP resonators. As previously discussed in Sec. II B, cavity losses primarily stem from imperfections in the fiber end facets, which vary depending on the type of fiber used. For example, chalcogenide fibers are very soft, while photonic crystal fibers feature numerous holes.[202] Consequently, it is crucial to employ new techniques for highly precise mechanical polishing and monitoring, as well as precise coatings consistent with the designed parameters. The second challenge relates to dispersion engineering in conventional fibers, where weakly confined large modes might limit the engineering capability. However, it is still feasible to engineer the cavity dispersion not only through material dispersion but also by different sizes and micro- and-nanostructures such as photonic crystal fiber,[202] chirped fiber Bragg gratings,[203] and chirped coatings. The third challenge pertains to the scaling and control of cavity length. While it is relatively straightforward to fabricate longer cavities to meet the requirements of various applications,[204,205] such as dual-comb spectroscopy and photonic analog-to-digital converters (ADCs), it is challenging to push the FSR of a fiber FP resonator to exceed 50 GHz. This limitation may arise from the overall thickness of the cavity becoming too thin for fabrication. Additionally, compared to their on-chip counterparts, new techniques are required to precisely control the FP cavity length for applications such as stimulated Brillouin laser generation and combs with precise repetition rate differences. The fourth challenge concerns the absence of fast-modulated cavity properties, which is particularly important for sensing applications like LiDAR.[30,206,207] One feasible approach is to introduce nested cavities [as shown in Fig. 17(d)], while another involves integrating electrically tunable materials inside the fiber FP cavity. However, the latter approach may lead to a reduction in the Q factor. With continued efforts to understand and control new phenomena in fiber FP microcavities, the community will continue to improve the performance of fiber microcombs and expand the already impressive range of microcomb applications.

ACKNOWLEDGMENTS

National Science Foundation (Grant Nos. ECCS 2048202 and OMA 2016244) and Office of Naval Research (Grant No. N00014-22-1-2224).

AUTHOR DECLARATIONS

Conflict of Interest

The authors have no conflicts to disclose.

Author Contributions

Jonathan Musgrave: Writing – original draft (equal); Writing – review & editing (equal). **Shu-Wei Huang**: Funding acquisition (lead); Writing – original draft (supporting); Writing – review & editing (lead). **Mingming Nie**: Conceptualization (lead); Supervision (lead); Writing – original draft (lead); Writing – review & editing (equal).

DATA AVAILABILITY

All data generated or analyzed during this study are available within the paper. Furthermore, source data will be made available on reasonable request.

NOMENCLATURE

$1/\tau_{ext}$	pump external coupling rate
A	intracavity field
A_B	backward wave
A_{eff}	effective mode area
A_F	forward wave
A_p	amplitude of the incident pump field
C	specific heat
c	speed of light
D_1	free spectral range
D_2	group velocity dispersion
dn/dT	thermo-optic coefficient
F	finesse
f	offset frequency
f_{rep}	repetition rate frequency
g	frequency shift of a resonant mode per photon
g_B	Brillouin gain coefficient
k_B	Boltzmann constant
L	cavity length
n	optical refractive index
n_2	Kerr coefficient
Q	total quality factor
Q_{ext}	external or coupling Q factor
R	reflectivity coefficient
S	normalized pump amplitude
$S_{\delta T}(f)$	thermodynamic fluctuations
$S_\nu(f)$	frequency noise
t	slow time
T	transmission coefficients
T_{em}	temperature
t_R	round-trip time
V	mode volume
Γ	spatial overlap factor
Γ_B	loss rate of the density wave (Brillouin gain bandwidth)
$\Delta\nu_{FSR}$	free spectral range
$\Delta\nu$	cavity linewidth
$\Delta\nu_0$	non-broadened SBL linewidth
$\Delta\tau$	soliton pulse width
Λ_B	mode overlaps of the backward wave
Λ_F	mode overlaps of the forward wave
Λ_ρ	mode overlaps of the density wave
Ω	actual frequency shift (between pump and SBL)
Ω_B	Brillouin frequency shift
α	propagation loss
α_i	intrinsic loss
α_o	output coupling loss
β	propagation constant
β_1	group velocity
β_2	group velocity dispersion

γ	Kerr nonlinear parameter
γ_e	electrostrictive constant
δ	detuning
δ_B	SBL detuning
δ_F	pump detuning
δ_ρ	acoustic wave detuning
ζ	linewidth broadening factor
η	loading efficiency
η_q	quantum efficiency of the detector
κ_{ex}	pump coupling coefficient
λ	wavelength in vacuum
ν	optical frequency
ρ	acoustic wave
ρ_0	density
τ	cavity photon lifetime
τ	fast time
τ_B	backward wave lifetime
τ_F	forward wave lifetime
υ_s	speed of sound
ϕ	optical phase
ψ	intracavity field
ω, ω_0	angular optical frequency
$\hbar$	Plank constant

REFERENCES

[1] S. A. Diddams, "The evolving optical frequency comb (invited)," J. Opt. Soc. Am. B **27**, B51–B62 (2010).

[2] A. Trabesinger, "Nobel prize 2005: Glauber, Hall and Hänsch," Nat. Phys. **1**, 930 (2005).

[3] P. Del'Haye, A. Schliesser, O. Arcizet, T. Wilken, R. Holzwarth, and T. J. Kippenberg, "Optical frequency comb generation from a monolithic microresonator," Nature **450**, 1214–1217 (2007).

[4] S. B. Papp, K. Beha, P. Del'Haye, F. Quinlan, H. Lee, K. J. Vahala, and S. A. Diddams, "Microresonator frequency comb optical clock," Optica **1**, 10–14 (2014).

[5] P. Del'Haye, A. Coillet, T. Fortier, K. Beha, D. C. Cole, K. Y. Yang, H. Lee, K. J. Vahala, S. B. Papp, and S. A. Diddams, "Phase-coherent microwave-to-optical link with a self-referenced microcomb," Nat. Photonics **10**, 516–520 (2016).

[6] Z. L. Newman, V. Maurice, T. Drake, J. R. Stone, T. C. Briles, D. T. Spencer, C. Fredrick, Q. Li, D. Westly, B. R. Ilic *et al.*, "Architecture for the photonic integration of an optical atomic clock," Optica **6**, 680–685 (2019).

[7] T. E. Drake, T. C. Briles, J. R. Stone, D. T. Spencer, D. R. Carlson, D. D. Hickstein, Q. Li, D. Westly, K. Srinivasan, S. A. Diddams, and S. B. Papp, "Terahertz-rate Kerr-microresonator optical clockwork," Phys. Rev. X **9**, 031023 (2019).

[8] S.-W. Huang, J. Yang, M. Yu, B. H. McGuyer, D.-L. Kwong, T. Zelevinsky, and C. W. Wong, "A broadband chip-scale optical frequency synthesizer at 2.7×10^{-16} relative uncertainty," Sci. Adv. **2**, e1501489 (2016).

[9] S. Arafin, A. Simsek, S.-K. Kim, S. Dwivedi, W. Liang, D. Eliyahu, J. Klamkin, A. Matsko, L. Johansson, L. Maleki *et al.*, "Towards chip-scale optical frequency synthesis based on optical heterodyne phase-locked loop," Opt. Express **25**, 681–695 (2017).

[10] D. T. Spencer, T. Drake, T. C. Briles, J. Stone, L. C. Sinclair, C. Fredrick, Q. Li, D. Westly, B. R. Ilic, A. Bluestone, N. Volet *et al.*, "An optical-frequency synthesizer using integrated photonics," Nature **557**, 81–85 (2018).

[11] L. Stern, J. R. Stone, S. Kang, D. C. Cole, M.-G. Suh, C. Fredrick, Z. Newman, K. Vahala, J. Kitching, S. A. Diddams, and S. B. Papp, "Direct Kerr frequency comb atomic spectroscopy and stabilization," Sci. Adv. **6**, eaax6230 (2020).

[12] M.-G. Suh, Q.-F. Yang, K. Y. Yang, X. Yi, and K. J. Vahala, "Microresonator soliton dual-comb spectroscopy," Science **354**, 600–603 (2016).

[13] Q.-F. Yang, B. Shen, H. Wang, M. Tran, Z. Zhang, K. Y. Yang, L. Wu, C. Bao, J. Bowers, A. Yariv, and K. Vahala, "Vernier spectrometer using counterpropagating soliton microcombs," Science **363**, 965–968 (2019).

[14] M. Yu, Y. Okawachi, A. G. Griffith, N. Picqué, M. Lipson, and A. L. Gaeta, "Silicon-chip-based mid-infrared dual-comb spectroscopy," Nat. Commun. **9**, 1869 (2018).

[15] M.-G. Suh, X. Yi, Y.-H. Lai, S. Leifer, I. S. Grudinin, G. Vasisht, E. C. Martin, M. P. Fitzgerald, G. Doppmann, J. Wang *et al.*, "Searching for exoplanets using a microresonator astrocomb," Nat. Photonics **13**, 25–30 (2019).

[16] E. Obrzud, M. Rainer, A. Harutyunyan, M. H. Anderson, J. Liu, M. Geiselmann, B. Chazelas, S. Kundermann, S. Lecomte, M. Cecconi *et al.*, "A microphotonic astrocomb," Nat. Photonics **13**, 31–35 (2019).

[17] X. Ji, X. Yao, A. Klenner, Y. Gan, A. L. Gaeta, C. P. Hendon, and M. Lipson, "Chip-based frequency comb sources for optical coherence tomography," Opt. Express **27**, 19896–19905 (2019).

[18] P. J. Marchand, J. Riemensberger, J. C. Skehan, J.-J. Ho, M. H. Pfeiffer, J. Liu, C. Hauger, T. Lasser, and T. J. Kippenberg, "Soliton microcomb based spectral domain optical coherence tomography," Nat. Commun. **12**, 427 (2021).

[19] C. Bao, M.-G. Suh, and K. Vahala, "Microresonator soliton dual-comb imaging," Optica **6**, 1110–1116 (2019).

[20] A. Jørgensen, D. Kong, M. Henriksen, F. Klejs, Z. Ye, Ò. Helgason, H. Hansen, H. Hu, M. Yankov, S. Forchhammer *et al.*, "Petabit-per-second data transmission using a chip-scale microcomb ring resonator source," Nat. Photonics **16**, 1–5 (2022).

[21] J. Pfeifle, V. Brasch, M. Lauermann, Y. Yu, D. Wegner, T. Herr, K. Hartinger, P. Schindler, J. Li, D. Hillerkuss, R. Schmogrow *et al.*, "Coherent terabit communications with microresonator Kerr frequency combs," Nat. Photonics **8**, 375–380 (2014).

[22] P. Marin-Palomo, J. N. Kemal, M. Karpov, A. Kordts, J. Pfeifle, M. H. Pfeiffer, P. Trocha, S. Wolf, V. Brasch, M. H. Anderson *et al.*, "Microresonator-based solitons for massively parallel coherent optical communications," Nature **546**, 274–279 (2017).

[23] A. Fülöp, M. Mazur, A. Lorences-Riesgo, T. A. Eriksson, P.-H. Wang, Y. Xuan, D. E. Leaird, M. Qi, P. A. Andrekson, A. M. Weiner, and V. Torres-Company, "Long-haul coherent communications using microresonator-based frequency combs," Opt. Express **25**, 26678–26688 (2017).

[24] P. Liao, C. Bao, A. Kordts, M. Karpov, M. H. Pfeiffer, L. Zhang, Y. Cao, A. Almaiman, A. Mohajerin-Ariaei, M. Tur *et al.*, "Pump-linewidth-tolerant wavelength multicasting using soliton Kerr frequency combs," Opt. Lett. **42**, 3177–3180 (2017).

[25] Y. Geng, X. Huang, W. Cui, Y. Ling, B. Xu, J. Zhang, X. Yi, B. Wu, S.-W. Huang, K. Qiu *et al.*, "Terabit optical OFDM superchannel transmission via coherent carriers of a hybrid chip-scale soliton frequency comb," Opt. Lett. **43**, 2406–2409 (2018).

[26] A. Fülöp, M. Mazur, A. Lorences-Riesgo, Ó. B. Helgason, P.-H. Wang, Y. Xuan, D. E. Leaird, M. Qi, P. A. Andrekson, and A. M. Weiner *et al.*, "High-order coherent communications using mode-locked dark-pulse Kerr combs from microresonators," Nat. Commun. **9**, 1598 (2018).

[27] M. Mazur, M.-G. Suh, A. Fulop, J. Schroder, V. Torres-Company, M. Karlsson, K. J. Vahala, and P. Andrekson, "High spectral efficiency coherent superchannel transmission with soliton microcombs," J. Lightwave Technol. **39**, 4367 (2021).

[28] M.-G. Suh and K. J. Vahala, "Soliton microcomb range measurement," Science **359**, 884–887 (2018).

[29] P. Trocha, M. Karpov, D. Ganin, M. H. Pfeiffer, A. Kordts, S. Wolf, J. Krockenberger, P. Marin-Palomo, C. Weimann, S. Randel *et al.*, "Ultrafast optical ranging using microresonator soliton frequency combs," Science **359**, 887–891 (2018).

[30] J. Riemensberger, A. Lukashchuk, M. Karpov, W. Weng, E. Lucas, J. Liu, and T. J. Kippenberg, "Massively parallel coherent laser ranging using a soliton microcomb," Nature **581**, 164–170 (2020).

[31] M. Kues, C. Reimer, J. M. Lukens, W. J. Munro, A. M. Weiner, D. J. Moss, and R. Morandotti, "Quantum optical microcombs," Nat. Photonics **13**, 170–179 (2019).

[32] C. Reimer, M. Kues, P. Roztocki, B. Wetzel, F. Grazioso, B. E. Little, S. T. Chu, T. Johnston, Y. Bromberg, L. Caspani *et al.*, "Generation of multiphoton entangled

quantum states by means of integrated frequency combs," Science **351**, 1176–1180 (2016).
[33]M. Kues, C. Reimer, P. Roztocki, L. R. Cortés, S. Sciara, B. Wetzel, Y. Zhang, A. Cino, S. T. Chu, B. E. Little *et al.*, "On-chip generation of high-dimensional entangled quantum states and their coherent control," Nature **546**, 622–626 (2017).
[34]P. Imany, J. A. Jaramillo-Villegas, O. D. Odele, K. Han, D. E. Leaird, J. M. Lukens, P. Lougovski, M. Qi, and A. M. Weiner, "50-GHz-spaced comb of high-dimensional frequency-bin entangled photons from an on-chip silicon nitride microresonator," Opt. Express **26**, 1825–1840 (2018).
[35]Z. Yang, M. Jahanbozorgi, D. Jeong, S. Sun, O. Pfister, H. Lee, and X. Yi, "A squeezed quantum microcomb on a chip," Nat. Commun. **12**, 4781 (2021).
[36]F.-X. Wang, W. Wang, R. Niu, X. Wang, C.-L. Zou, C.-H. Dong, B. E. Little, S. T. Chu, H. Liu, P. Hao, S. Liu, S. Wang, Z.-Q. Yin, D.-Y. He, W. Zhang, W. Zhao, Z.-F. Han, G.-C. Guo, and W. Chen, "Quantum key distribution with on-chip dissipative Kerr soliton," Laser Photonics Rev. **14**, 1900190 (2020).
[37]T. Herr, V. Brasch, J. D. Jost, C. Y. Wang, N. M. Kondratiev, M. L. Gorodetsky, and T. J. Kippenberg, "Temporal solitons in optical microresonators," Nat. Photonics **8**, 145–152 (2014).
[38]T. Herr, V. Brasch, J. Jost, I. Mirgorodskiy, G. Lihachev, M. Gorodetsky, and T. Kippenberg, "Mode spectrum and temporal soliton formation in optical microresonators," Phys. Rev. Lett. **113**, 123901 (2014).
[39]X. Yi, Q.-F. Yang, K. Y. Yang, M.-G. Suh, and K. Vahala, "Soliton frequency comb at microwave rates in a high-*Q* silica microresonator," Optica **2**, 1078–1085 (2015).
[40]H. Zhang, T. Tan, H.-J. Chen, Y. Yu, W. Wang, B. Chang, Y. Liang, Y. Guo, H. Zhou, H. Xia *et al.*, "Soliton microcombs multiplexing using intracavity-stimulated Brillouin lasers," Phys. Rev. Lett. **130**, 153802 (2023).
[41]M. Qu, C. Li, K. Liu, W. Zhu, Y. Wei, P. Wang, and S. Kang, "Soliton generation in CaF_2 crystalline whispering gallery mode resonators with negative thermal-optical effects," arXiv:2306.02128 (2023).
[42]Y. He, Q.-F. Yang, J. Ling, R. Luo, H. Liang, M. Li, B. Shen, H. Wang, K. Vahala, and Q. Lin, "Self-starting bi-chromatic $LiNbO_3$ soliton microcomb," Optica **6**, 1138–1144 (2019).
[43]X. Liu, Z. Gong, A. W. Bruch, J. B. Surya, J. Lu, and H. X. Tang, "Aluminum nitride nanophotonics for beyond-octave soliton microcomb generation and self-referencing," Nat. Commun. **12**, 5428 (2021).
[44]L. Wu, W. Xie, H.-J. Chen, K. Colburn, C. Xiang, L. Chang, W. Jin, J.-Y. Liu, Y. Yu, Y. Yamamoto *et al.*, "AlGaAs soliton microcombs at room temperature," Opt. Lett. **48**, 3853–3856 (2023).
[45]V. Brasch, M. Geiselmann, T. Herr, G. Lihachev, M. H. Pfeiffer, M. L. Gorodetsky, and T. J. Kippenberg, "Photonic chip-based optical frequency comb using soliton Cherenkov radiation," Science **351**, 357–360 (2016).
[46]C. Wang, J. Li, A. Yi, Z. Fang, L. Zhou, Z. Wang, R. Niu, Y. Chen, J. Zhang, Y. Cheng *et al.*, "Soliton formation and spectral translation into visible on CMOS-compatible 4H-silicon-carbide-on-insulator platform," Light: Sci. Appl. **11**, 341 (2022).
[47]D. Xia, Z. Yang, P. Zeng, B. Zhang, J. Wu, Z. Wang, J. Zhao, J. Huang, L. Luo, D. Liu *et al.*, "Integrated chalcogenide photonics for microresonator soliton combs," Laser Photonics Rev. **17**, 2200219 (2023).
[48]A. Nardi, A. Davydova, N. Kuznetsov, M. H. Anderson, C. Möhl, J. Riemensberger, T. J. Kippenberg, and P. Seidler, "Soliton microcomb generation in a III–V photonic crystal cavity," arXiv:2304.12968 (2023).
[49]E. Lucas, S.-P. Yu, T. C. Briles, D. R. Carlson, and S. B. Papp, "Tailoring microcombs with inverse-designed, meta-dispersion microresonators," Nat. Photonics **17**, 943–950 (2023).
[50]S.-P. Yu, D. C. Cole, H. Jung, G. T. Moille, K. Srinivasan, and S. B. Papp, "Spontaneous pulse formation in edgeless photonic crystal resonators," Nat. Photonics **15**, 461–467 (2021).
[51]T. Wildi, M. A. Gaafar, T. Voumard, M. Ludwig, and T. Herr, "Dissipative Kerr solitons in integrated Fabry–Perot microresonators," Optica **10**, 650–656 (2023).
[52]A. E. Ulanov, T. Wildi, N. G. Pavlov, J. D. Jost, M. Karpov, and T. Herr, "Synthetic-reflection self-injection-locked microcombs," arXiv:2301.13132 (2023).
[53]E. Obrzud, S. Lecomte, and T. Herr, "Temporal solitons in microresonators driven by optical pulses," Nat. Photonics **11**, 600–607 (2017).
[54]M. Nie, K. Jia, Y. Xie, S. Zhu, Z. Xie, and S.-W. Huang, "Synthesized spatiotemporal mode-locking and photonic flywheel in multimode mesoresonators," Nat. Commun. **13**, 6395 (2022).
[55]Z. Xiao, T. Li, M. Cai, H. Zhang, Y. Huang, C. Li, B. Yao, K. Wu, and J. Chen, "Near-zero-dispersion soliton and broadband modulational instability Kerr microcombs in anomalous dispersion," Light: Sci. Appl. **12**, 33 (2023).
[56]T. K. Gangopadhyay, "Prospects for fibre Bragg gratings and Fabry–Perot interferometers in fibre-optic vibration sensing," Sens. Actuators, A **113**, 20–38 (2004).
[57]M. Ding, M. Komanec, D. Suslov, D. Dousek, S. Zvánovec, E. R. N. Fokoua, T. D. Bradley, F. Poletti, D. J. Richardson, and R. Slavík, "Long-length and thermally stable high-finesse Fabry–Perot interferometers made of hollow core optical fiber," J. Lightwave Technol. **38**, 2423–2427 (2020).
[58]F. Leo, S. Coen, P. Kockaert, S.-P. Gorza, P. Emplit, and M. Haelterman, "Temporal cavity solitons in one-dimensional Kerr media as bits in an all-optical buffer," Nat. Photonics **4**, 471–476 (2010).
[59]Y. Xie, D. Cai, H. Wu, J. Pan, N. Zhou, C. Xin, S. Yu, P. Wang, X. Jiang, J. Qiu, X. Guo, and L. Tong, "Mid-infrared chalcogenide microfiber knot resonators," Photonics Res. **8**, 616–621 (2020).
[60]Z. Ding, Z. Huang, Y. Chen, C. Mou, Y. Lu, and F. Xu, "All-fiber ultrafast laser generating gigahertz-rate pulses based on a hybrid plasmonic microfiber resonator," Adv. Photonics **2**, 026002 (2020).
[61]D. Zixuan, C. Ye, and X. Fei, "Optical microfiber resonator: Principle and applications," Opto-Electron. Eng. **49**, 220006 (2022).
[62]D. Braje, L. Hollberg, and S. Diddams, "Brillouin-enhanced hyperparametric generation of an optical frequency comb in a monolithic highly nonlinear fiber cavity pumped by a cw laser," Phys. Rev. Lett. **102**, 193902 (2009).
[63]K. Jia, X. Wang, D. Kwon, J. Wang, E. Tsao, H. Liu, X. Ni, J. Guo, M. Yang, X. Jiang *et al.*, "Photonic flywheel in a monolithic fiber resonator," Phys. Rev. Lett. **125**, 143902 (2020).
[64]C. Qin, J. Du, T. Tan, B. Chang, K. Jia, Y. Liang, W. Wang, Y. Guo, H. Xia, S. Zhu *et al.*, "Co-generation of orthogonal soliton pair in a monolithic fiber resonator with mechanical tunability," Laser Photonics Rev. **17**, 2200662 (2023).
[65]B. H. Lee, Y. H. Kim, K. S. Park, J. B. Eom, M. J. Kim, B. S. Rho, and H. Y. Choi, "Interferometric fiber optic sensors," Sensors **12**, 2467–2486 (2012).
[66]T. Tan, Z. Yuan, H. Zhang, G. Yan, S. Zhou, N. An, B. Peng, G. Soavi, Y. Rao, and B. Yao, "Multispecies and individual gas molecule detection using Stokes solitons in a graphene over-modal microresonator," Nat. Commun. **12**, 6716 (2021).
[67]D. L. Franzen and E. M. Kim, "Long optical-fiber Fabry–Perot interferometers," Appl. Opt. **20**, 3991–3992 (1981).
[68]P. Cielo, "Fiber optic hydrophone: Improved strain configuration and environmental noise protection," Appl. Opt. **18**, 2933–2937 (1979).
[69]S. Petuchowski, T. Giallorenzi, and S. Sheem, "A sensitive fiber-optic Fabry–Perot interferometer," IEEE J. Quantum Electron. **17**, 2168–2170 (1981).
[70]M. Nie, B. Li, K. Jia, Y. Xie, J. Yan, S. Zhu, Z. Xie, and S.-W. Huang, "Dissipative soliton generation and real-time dynamics in microresonator-filtered fiber lasers," Light: Sci. Appl. **11**, 296 (2022).
[71]D. Marcuse, "Reflection loss of laser mode from tilted end mirror," J. Lightwave Technol. **7**, 336–339 (1989).
[72]L. Wu, H. Wang, Q. Yang, Q. Ji, B. Shen, C. Bao, M. Gao, and K. Vahala, "Greater than one billion Q factor for on-chip microresonators," Opt. Lett. **45**, 5129–5131 (2020).
[73]S. Fujii and T. Tanabe, "Dispersion engineering and measurement of whispering gallery mode microresonator for Kerr frequency comb generation," Nanophotonics **9** (2020).
[74]A. F. Runge, D. D. Hudson, K. K. Tam, C. M. de Sterke, and A. Blanco-Redondo, "The pure-quartic soliton laser," Nat. Photonics **14**, 492–497 (2020).
[75]C. M. de Sterke, A. F. Runge, D. D. Hudson, and A. Blanco-Redondo, "Pure-quartic solitons and their generalizations—Theory and experiments," APL Photonics **6**, 091101 (2021).
[76]L. A. Lugiato and R. Lefever, "Spatial dissipative structures in passive optical systems," Phys. Rev. Lett. **58**, 2209 (1987).
[77]S. Coen, H. G. Randle, T. Sylvestre, and M. Erkintalo, "Modeling of octave-spanning Kerr frequency combs using a generalized mean-field Lugiato–Lefever model," Opt. Lett. **38**, 37–39 (2013).

[78]C. Godey, I. V. Balakireva, A. Coillet, and Y. K. Chembo, "Stability analysis of the spatiotemporal Lugiato–Lefever model for Kerr optical frequency combs in the anomalous and normal dispersion regimes," Phys. Rev. A **89**, 063814 (2014).
[79]M. Nie and S.-W. Huang, "Quadratic soliton mode-locked degenerate optical parametric oscillator," Opt. Lett. **45**, 2311–2314 (2020).
[80]M. Nie and S.-W. Huang, "Quadratic solitons in singly resonant degenerate optical parametric oscillators," Phys. Rev. Appl. **13**, 044046 (2020).
[81]T. Hansson, D. Modotto, and S. Wabnitz, "On the numerical simulation of Kerr frequency combs using coupled mode equations," Opt. Commun. **312**, 134–136 (2014).
[82]C. Bao, Y. Xuan, J. A. Jaramillo-Villegas, D. E. Leaird, M. Qi, and A. M. Weiner, "Direct soliton generation in microresonators," Opt. Lett. **42**, 2519–2522 (2017).
[83]Y. Bai, M. Zhang, Q. Shi, S. Ding, Y. Qin, Z. Xie, X. Jiang, and M. Xiao, "Brillouin–Kerr soliton frequency combs in an optical microresonator," Phys. Rev. Lett. **126**, 063901 (2021).
[84]M. Anderson, F. Leo, S. Coen, M. Erkintalo, and S. G. Murdoch, "Observations of spatiotemporal instabilities of temporal cavity solitons," Optica **3**, 1071–1074 (2016).
[85]F. Leo, L. Gelens, P. Emplit, M. Haelterman, and S. Coen, "Dynamics of one-dimensional Kerr cavity solitons," Opt. Express **21**, 9180–9191 (2013).
[86]A. Dutt, K. Luke, S. Manipatruni, A. L. Gaeta, P. Nussenzveig, and M. Lipson, "On-chip optical squeezing," Phys. Rev. Appl. **3**, 044005 (2015).
[87]S.-W. Huang, J. Yang, S.-H. Yang, M. Yu, D.-L. Kwong, T. Zelevinsky, M. Jarrahi, and C. W. Wong, "Globally stable microresonator Turing pattern formation for coherent high-power THz radiation on-chip," Phys. Rev. X **7**, 041002 (2017).
[88]W. Wang, P.-K. Lu, A. K. Vinod, D. Turan, J. F. McMillan, H. Liu, M. Yu, D.-L. Kwong, M. Jarrahi, and C. W. Wong, "Coherent terahertz radiation with 2.8-octave tunability through chip-scale photomixed microresonator optical parametric oscillation," Nat. Commun. **13**, 5123 (2022).
[89]A. Lukashchuk, J. Riemensberger, A. Tusnin, J. Liu, and T. J. Kippenberg, "Chaotic microcomb-based parallel ranging," Nat. Photonics **17**, 814–821 (2023).
[90]R. Chen, H. Shu, B. Shen, L. Chang, W. Xie, W. Liao, Z. Tao, J. E. Bowers, and X. Wang, "Breaking the temporal and frequency congestion of LiDAR by parallel chaos," Nat. Photonics **17**, 306–314 (2023).
[91]B. Shen, H. Shu, W. Xie, R. Chen, Z. Liu, Z. Ge, X. Zhang, Y. Wang, Y. Zhang, B. Cheng, S. Yu *et al.*, "Harnessing microcomb-based parallel chaos for random number generation and optical decision making," Nat. Commun. **14**, 4590 (2023).
[92]C. Bao, J. A. Jaramillo-Villegas, Y. Xuan, D. E. Leaird, M. Qi, and A. M. Weiner, "Observation of Fermi–Pasta–Ulam recurrence induced by breather solitons in an optical microresonator," Phys. Rev. Lett. **117**, 163901 (2016).
[93]D. C. Cole and S. B. Papp, "Subharmonic entrainment of Kerr breather solitons," Phys. Rev. Lett. **123**, 173904 (2019).
[94]C. Bao, Y. Xuan, D. E. Leaird, S. Wabnitz, M. Qi, and A. M. Weiner, "Spatial mode-interaction induced single soliton generation in microresonators," Optica **4**, 1011–1015 (2017).
[95]X. Yi, Q.-F. Yang, K. Y. Yang, and K. Vahala, "Imaging soliton dynamics in optical microcavities," Nat. Commun. **9**, 3565 (2018).
[96]J. Li, C. Bao, Q.-X. Ji, H. Wang, L. Wu, S. Leifer, C. Beichman, and K. Vahala, "Efficiency of pulse pumped soliton microcombs," Optica **9**, 231–239 (2022).
[97]X. Xue, Y. Xuan, P.-H. Wang, Y. Liu, D. E. Leaird, M. Qi, and A. M. Weiner, "Normal-dispersion microcombs enabled by controllable mode interactions," Laser Photonics Rev. **9**, L23–L28 (2015).
[98]X. Xue, X. Zheng, and B. Zhou, "Super-efficient temporal solitons in mutually coupled optical cavities," Nat. Photonics **13**, 616–622 (2019).
[99]Z. Gong, A. W. Bruch, F. Yang, M. Li, J. Lu, J. B. Surya, C.-L. Zou, and H. X. Tang, "Quadratic strong coupling in AlN Kerr cavity solitons," Opt. Lett. **47**, 746–749 (2022).
[100]A. W. Bruch, X. Liu, Z. Gong, J. B. Surya, M. Li, C.-L. Zou, and H. X. Tang, "Pockels soliton microcomb," Nat. Photonics **15**, 21–27 (2021).
[101]H. Bao, A. Cooper, M. Rowley, L. Di Lauro, J. S. Totero Gongora, S. T. Chu, B. E. Little, G.-L. Oppo, R. Morandotti, D. J. Moss, B. Wetzel *et al.*, "Laser cavity-soliton microcombs," Nat. Photonics **13**, 384–389 (2019).
[102]P. Liao, C. Bao, A. Kordts, M. Karpov, M. H. Pfeiffer, L. Zhang, A. Mohajerin-Ariaei, Y. Cao, A. Almaiman, M. Ziyadi *et al.*, "Dependence of a microresonator Kerr frequency comb on the pump linewidth," Opt. Lett. **42**, 779–782 (2017).
[103]W. Jin, Q.-F. Yang, L. Chang, B. Shen, H. Wang, M. A. Leal, L. Wu, M. Gao, A. Feshali, M. Paniccia *et al.*, "Hertz-linewidth semiconductor lasers using CMOS-ready ultra-high-*Q* microresonators," Nat. Photonics **15**, 346–353 (2021).
[104]G. Huang, E. Lucas, J. Liu, A. S. Raja, G. Lihachev, M. L. Gorodetsky, N. J. Engelsen, and T. J. Kippenberg, "Thermorefractive noise in silicon-nitride microresonators," Phys. Rev. A **99**, 061801 (2019).
[105]Q.-F. Yang, Q.-X. Ji, L. Wu, B. Shen, H. Wang, C. Bao, Z. Yuan, and K. Vahala, "Dispersive-wave induced noise limits in miniature soliton microwave sources," Nat. Commun. **12**, 1442 (2021).
[106]K. H. Wanser, "Fundamental phase noise limit in optical fibres due to temperature fluctuations," Electron. Lett. **28**, 53 (1992).
[107]L. Duan, "General treatment of the thermal noises in optical fibers," Phys. Rev. A **86**, 023817 (2012).
[108]E. D. Black, "An introduction to Pound–Drever–Hall laser frequency stabilization," Am. J. Phys. **69**, 79–87 (2001).
[109]X. Yi, Q.-F. Yang, K. Youl Yang, and K. Vahala, "Active capture and stabilization of temporal solitons in microresonators," Opt. Lett. **41**, 2037–2040 (2016).
[110]E. Lucas, P. Brochard, R. Bouchand, S. Schilt, T. Südmeyer, and T. J. Kippenberg, "Ultralow-noise photonic microwave synthesis using a soliton microcomb-based transfer oscillator," Nat. Commun. **11**, 374 (2020).
[111]Q.-F. Yang, X. Yi, K. Y. Yang, and K. Vahala, "Spatial-mode-interaction-induced dispersive waves and their active tuning in microresonators," Optica **3**, 1132–1135 (2016).
[112]A. Yulin, R. Driben, B. Malomed, and D. Skryabin, "Soliton interaction mediated by cascaded four wave mixing with dispersive waves," Opt. Express **21**, 14481–14486 (2013).
[113]X. Yi, Q.-F. Yang, X. Zhang, K. Y. Yang, X. Li, and K. Vahala, "Single-mode dispersive waves and soliton microcomb dynamics," Nat. Commun. **8**, 14869 (2017).
[114]A. B. Matsko and L. Maleki, "On timing jitter of mode locked Kerr frequency combs," Opt. Express **21**, 28862–28876 (2013).
[115]Z. Xiao, K. Wu, T. Li, and J. Chen, "Deterministic single-soliton generation in a graphene-FP microresonator," Opt. Express **28**, 14933–14947 (2020).
[116]D. C. Cole, A. Gatti, S. B. Papp, F. Prati, and L. Lugiato, "Theory of Kerr frequency combs in Fabry–Perot resonators," Phys. Rev. A **98**, 013831 (2018).
[117]G. N. Campbell, L. Hill, P. Del'Haye, and G.-L. Oppo, "Dark solitons in Fabry–Perot resonators with Kerr media and normal dispersion," arXiv:2306.02946 (2023).
[118]Z. Ziani, T. Bunel, A. M. Perego, A. Mussot, and M. Conforti, "Theory of modulation instability in Kerr Fabry–Perot resonators beyond the mean field limit," arXiv:2307.13488 (2023).
[119]Q. Li, T. C. Briles, D. A. Westly, T. E. Drake, J. R. Stone, B. R. Ilic, S. A. Diddams, S. B. Papp, and K. Srinivasan, "Stably accessing octave-spanning microresonator frequency combs in the soliton regime," Optica **4**, 193–203 (2017).
[120]H. Zhou, Y. Geng, W. Cui, S.-W. Huang, Q. Zhou, K. Qiu, and C. Wei Wong, "Soliton bursts and deterministic dissipative Kerr soliton generation in auxiliary-assisted microcavities," Light: Sci. Appl. **8**, 50–10 (2019).
[121]B. Shen, L. Chang, J. Liu, H. Wang, Q.-F. Yang, C. Xiang, R. N. Wang, J. He, T. Liu, W. Xie *et al.*, "Integrated turnkey soliton microcombs," Nature **582**, 365–369 (2020).
[122]M. Nie, K. Jia, J. Bartos, S. Zhu, Z. Xie, and S.-W. Huang, "Turnkey photonic flywheel in a Chimera cavity," arXiv:2212.14120 (2022).
[123]H. Weng, J. Liu, A. A. Afridi, J. Li, J. Dai, X. Ma, Y. Zhang, Q. Lu, J. F. Donegan, and W. Guo, "Directly accessing octave-spanning dissipative Kerr soliton frequency combs in an AlN microresonator," Photonics Res. **9**, 1351–1357 (2021).
[124]G. Lihachev, W. Weng, J. Liu, L. Chang, J. Guo, J. He, R. N. Wang, M. H. Anderson, Y. Liu, J. E. Bowers, and T. J. Kippenberg, "Platicon microcomb generation using laser self-injection locking," Nat. Commun. **13**, 1771 (2022).
[125]L. Sirleto, A. Vergara, and M. A. Ferrara, "Advances in stimulated Raman scattering in nanostructures," Adv. Opt. Photonics **9**, 169–217 (2017).

[126]K. Lee, B. Sussman, M. Sprague, P. Michelberger, K. Reim, J. Nunn, N. Langford, P. Bustard, D. Jaksch, and I. Walmsley, "Macroscopic non-classical states and terahertz quantum processing in room-temperature diamond," Nat. Photonics **6**, 41–44 (2012).
[127]L. Rishøj, B. Tai, P. Kristensen, and S. Ramachandran, "Soliton self-mode conversion: Revisiting Raman scattering of ultrashort pulses," Optica **6**, 304–308 (2019).
[128]P. Latawiec, V. Venkataraman, M. J. Burek, B. J. Hausmann, I. Bulu, and M. Lončar, "On-chip diamond Raman laser," Optica **2**, 924–928 (2015).
[129]R. Suzuki, A. Kubota, A. Hori, S. Fujii, and T. Tanabe, "Broadband gain induced Raman comb formation in a silica microresonator," J. Opt. Soc. Am. B **35**, 933–938 (2018).
[130]X. Liu, C. Sun, B. Xiong, L. Wang, J. Wang, Y. Han, Z. Hao, H. Li, Y. Luo, J. Yan, T. Wei *et al.*, "Integrated continuous-wave aluminum nitride Raman laser," Optica **4**, 893–896 (2017).
[131]M. Yu, Y. Okawachi, R. Cheng, C. Wang, M. Zhang, A. L. Gaeta, and M. Lončar, "Raman lasing and soliton mode-locking in lithium niobate microresonators," Light: Sci. Appl. **9**, 9 (2020).
[132]Y. Wang, M. Anderson, S. Coen, S. G. Murdoch, and M. Erkintalo, "Stimulated Raman scattering imposes fundamental limits to the duration and bandwidth of temporal cavity solitons," Phys. Rev. Lett. **120**, 053902 (2018).
[133]Y. Okawachi, M. Yu, V. Venkataraman, P. M. Latawiec, A. G. Griffith, M. Lipson, M. Lončar, and A. L. Gaeta, "Competition between Raman and Kerr effects in microresonator comb generation," Opt. Lett. **42**, 2786–2789 (2017).
[134]Z. Gong, M. Li, X. Liu, Y. Xu, J. Lu, A. Bruch, J. B. Surya, C. Zou, and H. X. Tang, "Photonic dissipation control for Kerr soliton generation in strongly Raman-active media," Phys. Rev. Lett. **125**, 183901 (2020).
[135]Q.-F. Yang, X. Yi, K. Y. Yang, and K. Vahala, "Stokes solitons in optical microcavities," Nat. Phys. **13**, 53–57 (2017).
[136]Z. Li, Y. Xu, S. Shamailov, X. Wen, W. Wang, X. Wei, Z. Yang, S. Coen, S. G. Murdoch, and M. Erkintalo, "Ultrashort dissipative Raman solitons in Kerr resonators driven with phase-coherent optical pulses," arXiv:221208223 (2022).
[137]I. H. Do, D. Suk, D. Jeong, S. Go, K. Ko, H.-G. Hong, D.-H. Yu, J. H. Lee, and H. Lee, "Spontaneous soliton mode-locking of a microcomb assisted by Raman scattering," Opt. Express **31**, 29321–29330 (2023).
[138]M. Merklein, I. V. Kabakova, A. Zarifi, and B. J. Eggleton, "100 years of Brillouin scattering: Historical and future perspectives," Appl. Phys. Rev. **9**, 041306 (2022).
[139]M. O. Van Deventer and A. J. Boot, "Polarization properties of stimulated Brillouin scattering in single-mode fibers," J. Lightwave Technol. **12**, 585–590 (1994).
[140]M. Nie, K. Jia, S. Zhu, Z. Xie, and S.-W. Huang, "Noise-squeezed forward Brillouin lasers in multimode fiber microresonators," arXiv:2212.14122 (2022).
[141]A. Zadok, E. Zilka, A. Eyal, L. Thévenaz, and M. Tur, "Vector analysis of stimulated Brillouin scattering amplification in standard single-mode fibers," Opt. Express **16**, 21692–21707 (2008).
[142]I. S. Grudinin, A. B. Matsko, and L. Maleki, "Brillouin lasing with a CaF_2 whispering gallery mode resonator," Phys. Rev. Lett. **102**, 043902 (2009).
[143]J. Li, H. Lee, T. Chen, and K. J. Vahala, "Characterization of a high coherence, Brillouin microcavity laser on silicon," Opt. Express **20**, 20170–20180 (2012).
[144]D. Jin, Z. Bai, Y. Chen, W. Fan, Y. Wang, Z. Lü, and R. P. Mildren, "Intrinsic cascade-free intramode scattering Brillouin laser," APL Photonics **8**, 086107 (2023).
[145]K. Liu, M. W. Harrington, K. D. Nelson, R. O. Behunin, S. B. Papp, and D. J. Blumenthal, "Photonic integrated cascade-inhibited Brillouin laser with sub-100-mHz fundamental linewidth," in *CLEO Sci. Innov.* (Optica Publishing Group, 2022), p. SF2K-1.
[146]M. Merklein, I. V. Kabakova, T. F. Büttner, D.-Y. Choi, B. Luther-Davies, S. J. Madden, and B. J. Eggleton, "Enhancing and inhibiting stimulated Brillouin scattering in photonic integrated circuits," Nat. Commun. **6**, 6396 (2015).
[147]M. Puckett, D. Bose, K. Nelson, and D. J. Blumenthal, "Higher order cascaded SBS suppression using gratings in a photonic integrated ring resonator laser," in *CLEO Sci. Innov.* (Optica Publishing Group, 2019), p. SM4O-1.
[148]W. Loh, S. B. Papp, and S. A. Diddams, "Noise and dynamics of stimulated-Brillouin-scattering microresonator lasers," Phys. Rev. A **91**, 053843 (2015).
[149]A. Debut, S. Randoux, and J. Zemmouri, "Linewidth narrowing in Brillouin lasers: Theoretical analysis," Phys. Rev. A **62**, 023803 (2000).
[150]Z. Yuan, H. Wang, L. Wu, M. Gao, and K. Vahala, "Linewidth enhancement factor in a microcavity Brillouin laser," Optica **7**, 1150–1153 (2020).
[151]N. T. Otterstrom, R. O. Behunin, E. A. Kittlaus, Z. Wang, and P. T. Rakich, "A silicon Brillouin laser," Science **360**, 1113–1116 (2018).
[152]T. F. Büttner, I. V. Kabakova, D. D. Hudson, R. Pant, C. G. Poulton, A. C. Judge, and B. J. Eggleton, "Phase-locking and pulse generation in multi-frequency Brillouin oscillator via four wave mixing," Sci. Rep. **4**, 5032 (2014).
[153]M. Dong and H. G. Winful, "Unified approach to cascaded stimulated Brillouin scattering and frequency-comb generation," Phys. Rev. A **93**, 043851 (2016).
[154]T. F. Büttner, M. Merklein, I. V. Kabakova, D. D. Hudson, D.-Y. Choi, B. Luther-Davies, S. J. Madden, and B. J. Eggleton, "Phase-locked, chip-based, cascaded stimulated Brillouin scattering," Optica **1**, 311–314 (2014).
[155]I. H. Do, D. Kim, D. Jeong, D. Suk, D. Kwon, J. Kim, J. H. Lee, and H. Lee, "Self-stabilized soliton generation in a microresonator through mode-pulled Brillouin lasing," Opt. Lett. **46**, 1772–1775 (2021).
[156]Y. Zhao, L. Chen, C. Zhang, W. Wang, H. Hu, R. Wang, X. Wang, S. T. Chu, B. Little, W. Zhang, and X. Zhang, "Soliton burst and bi-directional switching in the platform with positive thermal-refractive coefficient using an auxiliary laser," Laser Photonics Rev. **15**, 2100264 (2021).
[157]M. Nie and S.-W. Huang, "Dissipative Kerr soliton induced by intermodal cascaded stimulated Brillouin scattering in graded-index multimode fiber Fabry–Pérot microresonators," in *CLEO Sci. Innov.* (Optical Society of America, 2022), p. STu1C-5.
[158]F. Lei, Z. Ye, Ó.B. Helgason, A. Fülöp, M. Girardi, and V. Torres-Company, "Optical linewidth of soliton microcombs," Nat. Commun. **13**, 3161 (2022).
[159]D. Kwon, C.-G. Jeon, J. Shin, M.-S. Heo, S. E. Park, Y. Song, and J. Kim, "Reference-free, high-resolution measurement method of timing jitter spectra of optical frequency combs," Sci. Rep. **7**, 40917 (2017).
[160]D. Jeong, D. Kwon, I. Jeon, I. H. Do, J. Kim, and H. Lee, "Ultralow jitter silica microcomb," Optica **7**, 1108–1111 (2020).
[161]S. Yao, Z. Wei, Y. Guo, L. Zhang, J. Wang, J. Yan, C. Bao, and C. Yang, "Self-frequency shift of AlN-on-sapphire Kerr solitons," Opt. Lett. **46**, 5312–5315 (2021).
[162]R. Shelby, M. Levenson, and P. Bayer, "Resolved forward Brillouin scattering in optical fibers," Phys. Rev. Lett. **54**, 939 (1985).
[163]R. Shelby, M. Levenson, and P. Bayer, "Guided acoustic-wave Brillouin scattering," Phys. Rev. B **31**, 5244 (1985).
[164]K. Smith and L. F. Mollenauer, "Experimental observation of soliton interaction over long fiber paths: Discovery of a long-range interaction," Opt. Lett. **14**, 1284–1286 (1989).
[165]J. K. Jang, M. Erkintalo, S. G. Murdoch, and S. Coen, "Ultraweak long-range interactions of solitons observed over astronomical distances," Nat. Photonics **7**, 657–663 (2013).
[166]M. Erkintalo, K. Luo, J. K. Jang, S. Coen, and S. G. Murdoch, "Bunching of temporal cavity solitons via forward Brillouin scattering," New J. Phys. **17**, 115009 (2015).
[167]C. Hilweg, D. Shadmany, P. Walther, N. Mavalvala, and V. Sudhir, "Limits and prospects for long-baseline optical fiber interferometry," Optica **9**, 1238–1252 (2022).
[168]M. Pang, W. He, X. Jiang, and P. S. J. Russell, "All-optical bit storage in a fibre laser by optomechanically bound states of solitons," Nat. Photonics **10**, 454–458 (2016).
[169]W. He, M. Pang, D.-H. Yeh, J. Huang, and P. S. J. Russell, "Synthesis and dissociation of soliton molecules in parallel optical-soliton reactors," Light: Sci. Appl. **10**, 120 (2021).
[170]M. Pang, X. Jiang, W. He, G. Wong, G. Onishchukov, N. Joly, G. Ahmed, C. Menyuk, and P. S. J. Russell, "Stable subpicosecond soliton fiber laser passively mode-locked by gigahertz acoustic resonance in photonic crystal fiber core," Optica **2**, 339–342 (2015).
[171]S. Kimura, S. Tani, and Y. Kobayashi, "Kerr-lens mode locking above a 20 GHz repetition rate," Optica **6**, 532–533 (2019).
[172]Z.-C. Luo, M. Liu, H. Liu, X.-W. Zheng, A.-P. Luo, C.-J. Zhao, H. Zhang, S.-C. Wen, and W.-C. Xu, "2 GHz passively harmonic mode-locked fiber laser

by a microfiber-based topological insulator saturable absorber," Opt. Lett. **38**, 5212–5215 (2013).
[173]A. Takada and H. Miyazawa, "30 GHz picosecond pulse generation from actively mode-locked erbium-doped fibre laser," Electron. Lett. **26**, 216–217 (1990).
[174]S. Yamashita, Y. Inoue, K. Hsu, T. Kotake, H. Yaguchi, D. Tanaka, M. Jablonski, and S. Y. Set, "5-GHz pulsed fiber Fabry–Pérot laser mode-locked using carbon nanotubes," IEEE Photonics Technol. Lett. **17**, 750–752 (2005).
[175]Y.-W. Song, S. Yamashita, C. S. Goh, and S. Y. Set, "Passively mode-locked lasers with 172-GHz fundamental-mode repetition rate pulsed by carbon nanotubes," Opt. Lett. **32**, 430–432 (2007).
[176]A. Martinez and S. Yamashita, "10 GHz fundamental mode fiber laser using a graphene saturable absorber," Appl. Phys. Lett. **101**, 041118 (2012).
[177]C. Qin, K. Jia, Q. Li, T. Tan, X. Wang, Y. Guo, S.-W. Huang, Y. Liu, S. Zhu, Z. Xie *et al.*, "Electrically controllable laser frequency combs in graphene-fibre microresonators," Light: Sci. Appl. **9**, 185 (2020).
[178]W. Lin, X. Chen, X. Hu, T. Luo, Y. Fan, W. Wang, Z. Liang, L. Ling, M. Hao, X. Wei, and Z. Yang, "Manipulating the polarization dynamics in a >10-GHz Er^{3+}/Yb^{3+} fiber Fabry–Pérot laser," Opt. Express **30**, 32791–32807 (2022).
[179]H. Cheng, W. Wang, Y. Zhou, T. Qiao, W. Lin, S. Xu, and Z. Yang, "5 GHz fundamental repetition rate, wavelength tunable, all-fiber passively mode-locked Yb-fiber laser," Opt. Express **25**, 27646–27651 (2017).
[180]Z. Liang, W. Lin, J. Wu, X. Chen, Y. Guo, L. Ling, X. Wei, and Z. Yang, ">10 GHz femtosecond fiber laser system at 2.0 μm," Opt. Lett. **47**, 1867–1870 (2022).
[181]N. Englebert, C. M. Arabí, P. Parra-Rivas, S.-P. Gorza, and F. Leo, "Temporal solitons in a coherently driven active resonator," Nat. Photonics **15**, 536 (2021).
[182]T. Tan, H.-J. Chen, Z. Yuan, Y. Yu, Q.-T. Cao, N. An, Q. Gong, C. W. Wong, Y. Rao, Y.-F. Xiao, and B. Yao, "Gain-assisted chiral soliton microcombs," arXiv:2008.12510 (2020).
[183]L. Columbo, M. Piccardo, F. Prati, L. Lugiato, M. Brambilla, A. Gatti, C. Silvestri, M. Gioannini, N. Opačak, B. Schwarz, and F. Capasso, "Unifying frequency combs in active and passive cavities: Temporal solitons in externally driven ring lasers," Phys. Rev. Lett. **126**, 173903 (2021).
[184]F. Prati, M. Brambilla, M. Piccardo, L. L. Columbo, C. Silvestri, M. Gioannini, A. Gatti, L. A. Lugiato, and F. Capasso, "Soliton dynamics of ring quantum cascade lasers with injected signal," Nanophotonics **10**, 195–207 (2020).
[185]B. Meng, M. Singleton, J. Hillbrand, M. Franckié, M. Beck, and J. Faist, "Dissipative Kerr solitons in semiconductor ring lasers," Nat. Photonics **16**, 142 (2021).
[186]L. L. Columbo, S. Barbieri, C. Sirtori, and M. Brambilla, "Dynamics of a broad-band quantum cascade laser: From chaos to coherent dynamics and mode-locking," Opt. Express **26**, 2829–2847 (2018).
[187]V. Vassiliev, V. Velichansky, V. Ilchenko, M. Gorodetsky, L. Hollberg, and A. Yarovitsky, "Narrow-line-width diode laser with a high-*Q* microsphere resonator," Opt. Commun. **158**, 305–312 (1998).
[188]W. Liang, V. Ilchenko, A. Savchenkov, A. Matsko, D. Seidel, and L. Maleki, "Whispering-gallery-mode-resonator-based ultranarrow linewidth external-cavity semiconductor laser," Opt. Lett. **35**, 2822–2824 (2010).
[189]W. Liang, V. Ilchenko, D. Eliyahu, A. Savchenkov, A. Matsko, D. Seidel, and L. Maleki, "Ultralow noise miniature external cavity semiconductor laser," Nat. Commun. **6**, 7371 (2015).
[190]E. Rivera-Pérez, A. Díez, M. Andrés, J. Cruz, and A. Rodríguez-Cobos, "Tunable narrowband fiber laser with feedback based on whispering gallery mode resonances of a cylindrical microresonator," Opt. Lett. **38**, 1636–1638 (2013).
[191]M. Peccianti, A. Pasquazi, Y. Park, B. E. Little, S. T. Chu, D. J. Moss, and R. Morandotti, "Demonstration of a stable ultrafast laser based on a nonlinear microcavity," Nat. Commun. **3**, 765 (2012).
[192]M. Rowley, P.-H. Hanzard, A. Cutrona, H. Bao, S. T. Chu, B. E. Little, R. Morandotti, D. J. Moss, G.-L. Oppo, J. S. Totero Gongora *et al.*, "Self-emergence of robust solitons in a microcavity," Nature **608**, 303–309 (2022).
[193]B. Y. Kim, Y. Okawachi, J. K. Jang, M. Yu, X. Ji, Y. Zhao, C. Joshi, M. Lipson, and A. L. Gaeta, "Turn-key, high-efficiency Kerr comb source," Opt. Lett. **44**, 4475–4478 (2019).
[194]D. Grassani, H. El Dirani, F. Sabattoli, L. Youssef, C. Petit-Etienne, S. Kerdiles, E. Pargon, M. Liscidini, C. Sciancalepore, D. Bajoni, and M. Galli, "Extending thermal stability of short-living soliton states in silicon nitride microring resonators," Opt. Continuum **1**, 1516–1528 (2022).
[195]N. Englebert, F. De Lucia, P. Parra-Rivas, C. M. Arabí, P.-J. Sazio, S.-P. Gorza, and F. Leo, "Parametrically driven Kerr cavity solitons," Nat. Photonics **15**, 857–861 (2021).
[196]M. Nie, Y. Xie, and S.-W. Huang, "Deterministic generation of parametrically driven dissipative Kerr soliton," Nanophotonics **10**, 1691–1699 (2021).
[197]X. Zeng, P. S. J. Russell, Y. Chen, Z. Wang, G. K. Wong, P. Roth, M. H. Frosz, and B. Stiller, "Optical vortex Brillouin laser," Laser Photonics Rev. **17**, 2200277 (2023).
[198]V. Krishna Inavalli and N. K. Viswanathan, "Switchable vector vortex beam generation using an optical fiber," Opt. Commun. **283**, 861–864 (2010).
[199]E. L. Bancel, E. Genier, R. Santagata, A. Kudlinski, M. Conforti, G. Bouwmans, O. Vanvincq, A. Cassez, and A. Mussot, "All-fiber triple frequency comb light source," in *CLEO Fundam. Sci.* (Optica Publishing Group, 2023), p. FW3B-5.
[200]P. Vaiano, B. Carotenuto, M. Pisco, A. Ricciardi, G. Quero, M. Consales, A. Crescitelli, E. Esposito, and A. Cusano, "Lab on fiber technology for biological sensing applications," Laser Photonics Rev. **10**, 922–961 (2016).
[201]Y. Xiong and F. Xu, "Multifunctional integration on optical fiber tips: Challenges and opportunities," Adv. Photonics **2**, 064001 (2020).
[202]J. C. Knight, "Photonic crystal fibres," Nature **424**, 847–851 (2003).
[203]K. Hill, K. Takiguchi, F. Bilodeau, B. Malo, T. Kitagawa, S. Thériault, D. C. Johnson, and J. Albert, "Chirped in-fiber Bragg gratings for compensation of optical-fiber dispersion," Opt. Lett. **19**, 1314–1316 (1994).
[204]N. Hoghooghi, S. Xing, P. Chang, D. Lesko, A. Lind, G. Rieker, and S. Diddams, "Broadband 1-GHz mid-infrared frequency comb," Light: Sci. Appl. **11**, 264 (2022).
[205]M.-G. Suh and K. Vahala, "Gigahertz-repetition-rate soliton microcombs," Optica **5**, 65–66 (2018).
[206]J. Liu, H. Tian, E. Lucas, A. S. Raja, G. Lihachev, R. N. Wang, J. He, T. Liu, M. H. Anderson, W. Weng, S. A. Bhave, and T. J. Kippenberg, "Monolithic piezoelectric control of soliton microcombs," Nature **583**, 385–390 (2020).
[207]Y. He, R. Lopez-Rios, U. A. Javid, J. Ling, M. Li, S. Xue, K. Vahala, and Q. Lin, "High-speed tunable microwave-rate soliton microcomb," Nat. Commun. **14**, 3467 (2023).